Late summer transition from a free-tropospheric to boundary layer source of Aitken mode aerosol in the high Arctic

Ruth Price[1], Andrea Baccarini[2,*], Julia Schmale[2], Paul Zieger[3,4], Ian M. Brooks[1], Paul Field[1,5], and Ken S. Carslaw[1]

[1]School of Earth and Environment, University of Leeds, Leeds, UK
[2]Extreme Environments Research Laboratory, École Polytechnique Fédérale de Lausanne, Sion, Switzerland
[3]Department of Environmental Science, Stockholm University, Stockholm, Sweden
[4]Bolin Centre for Climate Research, Stockholm University, Stockholm, Sweden
[5]Met Office, Exeter, UK
[*]now at: Laboratory of Atmospheric Processes and their Impacts, École Polytechnique Fédérale de Lausanne, Lausanne, Switzerland

Correspondence: Ruth Price (eersp@leeds.ac.uk)

Abstract. In the Arctic, the aerosol budget plays a particular role in determining the behaviour of clouds, which are important for the surface energy balance and thus for the region's climate. A key question is the extent to which cloud condensation nuclei in the high Arctic summertime boundary layer are controlled by local emission and formation processes as opposed to transport from outside. Each of these sources is likely to respond differently to future changes in ice cover. Here we use a global model
5 and observations from ship and aircraft field campaigns to understand the source of high Arctic aerosol in late summer. We find that particles formed remotely, i.e. at lower latitudes, outside the Arctic, are the dominant source of boundary layer Aitken mode particles during the sea ice melt period up to the end of August. Particles from such remote sources, entrained into the boundary layer from the free troposphere, account for nucleation and Aitken mode particle concentrations that are otherwise underestimated by the model. This source from outside the high Arctic declines as photochemical rates decrease towards the
10 end of summer, and is largely replaced by local new particle formation driven by iodic acid emitted from the surface and associated with freeze-up. Such a local source is consistent with strong fluctuations in nucleation mode concentrations that occur in September. Our results suggest a high-Arctic aerosol regime shift in late summer, and only after this shift do cloud condensation nuclei become sensitive to local aerosol processes.

1 Introduction

15 The Arctic is a key component of the global climate system. Over the past five decades, the mean surface temperature of the Arctic has increased 3–4 times faster than the global average (AMAP, 2021; Rantanen et al., 2022). Regional changes in the Arctic can have global impacts, such as climate feedbacks from albedo changes due to loss of sea ice, land ice and snow (Notz and Stroeve, 2018; Zhang et al., 2019; Flanner et al., 2011); changes in carbon sources due to increased wildfires (Walker et al., 2019; Randerson et al., 2006) and melting permafrost (Hugelius et al., 2014; Biskaborn et al., 2019); and global sea level rise
20 from melting of the Greenland ice sheet (Cazenave et al., 2018; Shepherd et al., 2012).

Clouds are a major control on the surface energy balance in the Arctic. Due to the low solar insolation and high albedo of sea ice in the high Arctic, the shortwave cooling effect of clouds is less important than at lower latitudes. Instead, longwave effects dominate such that the net radiative effect of low-level Arctic clouds is surface warming for all but a few weeks in the middle of summer (Curry et al., 1993; Shupe and Intrieri, 2004; Sedlar et al., 2011; Kay et al., 2016). Low clouds are common and

25   can persist in the mixed-phase for several days (Shupe, 2011). Aerosol particles act as cloud condensation nuclei (CCN) and ice-nucleating particles (INP) and therefore influence the behaviour of clouds. Observational Arctic case studies have shown that perturbations to aerosol concentrations can change the radiative effect of clouds (Lubin and Vogelmann, 2006; Garrett and Zhao, 2006; Mauritsen et al., 2011). Modelling studies reproduce this behaviour, while also highlighting the difficulty in creating models that can accurately simulate the complex behaviour of Arctic clouds (Alterskjær et al., 2010; Birch et al., 2012;

30   Stevens et al., 2018).

The aerosol budget of the high Arctic is a balance of different processes, including natural and anthropogenic primary emissions, new particle formation, condensational growth from vapours, long-range transport, and wet scavenging (Willis et al., 2018; Schmale et al., 2021). Transport of aerosol from lower latitudes is more efficient during the winter and spring because it is thermodynamically easier in winter for air to enter the Arctic region from the south than it is in summer (Stohl,

35   2006). Also, the removal of aerosol by frozen precipitation in winter is less effective than removal by drizzle in summer (Browse et al., 2012; Korhonen et al., 2008b). These seasonal cycles of aerosol transport and removal efficiency results in a transition from Arctic haze in the spring to more pristine conditions in the summer with fewer accumulation mode particles and more, smaller nucleation and Aitken mode particles (Engvall et al., 2008; Ström et al., 2003; Stohl, 2006; Tunved et al., 2013; Schmale et al., 2022).

40   Unlike the winter, when long-range transport is the dominant source of Arctic aerosols, summertime particles are thought to be strongly controlled by new particle formation (NPF) and growth from precursor vapours, which takes place in many Arctic locations. However, the large variety of vapours that can play a role, as well as the strong seasonal variation in key processes, have made it difficult to understand the main drivers of Arctic NPF. Observations of Arctic NPF are discussed in Schmale and Baccarini (2021) and will be briefly summarised here. Sulphuric acid (H_2SO_4) and methanesulphonic acid (MSA) have been

45   shown to drive NPF and growth in regions close to or influenced by open water such as Svalbard and the Canadian Arctic archipelago (Beck et al., 2020; Chang et al., 2011; Willis et al., 2017). The marine biogenic precursor dimethylsulphide (DMS) is the main source of H_2SO_4 and MSA to these regions. Open water is also a source of organic vapours which are observed to contribute to condensational growth of small particles (Willis et al., 2017). Ammonia has biogenic sources in the Arctic, for example seabird colonies, and has been observed to contribute to NPF events in Svalbard and Greenland (Croft et al., 2016;

50   Beck et al., 2020). Iodic acid (HIO_3) is known to be emitted from kelp in coastal areas and has been observed to drive NPF events near the coast of Greenland (Sipil a et al., 2016; Allan et al., 2015). Of relevance to this study, Baccarini et al. (2020a) recently observed iodic acid-driven NPF in the pack ice region of the Arctic Ocean during the sea ice freeze-up, suggesting an iodic acid source from snow, ice or ocean water.

Modelling studies have demonstrated the importance of NPF for the budget of Arctic aerosol. Merikanto et al. (2009) and

55   Gordon et al. (2017) used the global aerosol model GLOMAP to show the importance of NPF on a global scale. Both studies

indicate that a high fraction (greater than 80%) of particles and CCN in the Arctic are derived from new particle formation. While the model configuration in Merikanto et al. (2009) only included paremeterisations based on H_2SO_4, the model used by Gordon et al. (2017) included parameterisations for neutral and ion-induced binary (H_2SO_4-water) and ternary (H_2SO_4-ammonia-water) NPF, NPF from organic molecules and H_2SO_4, and pure organic NPF driven by highly oxygenated molecules

60 (HOMs). The authors found that a significant fraction (greater than 40%) of Arctic CCN originate from secondary organic aerosol, including HOMs. Karl et al. (2012) used an aerosol dynamics model to study NPF events that were observed during the summers of 1996, 2001 and 2008. H_2SO_4 and organic vapours were used in the model to drive NPF events. Simulations of NPF driven by H_2SO_4 followed by growth from condensation of organic vapours were able to reproduce the particle size distributions observed during NPF events. The inclusion of organic vapours as a driver of NPF led to an overprediction in the

65 concentration of particles, though the authors note significant uncertainty in the sources and concentrations of organic vapours in the high Arctic. Croft et al. (2019) used a chemical transport and aerosol microphysics model to show that condensation of secondary organic vapour played a key role in particle formation events in the Canadian Arctic during the summer. The vapours were assumed to have a marine, biogenic source. Browse et al. (2014), using GLOMAP to investigate the response of Arctic aerosol to sea ice loss, found that boundary layer NPF driven by H_2SO_4 was required to explain measured CCN concentrations

70 in the high Arctic during summer.

Boundary layer NPF as a source of Arctic aerosol implies a potentially high sensitivity of the local aerosol budget to the changing climate. Any future increase in the extent of open water and the marginal ice zone in summer will affect the emission of aerosol and precursor gases to the atmosphere. Dall'Osto et al. (2017, 2018) have found a correlation between frequency of NPF events and the extent of open water near Svalbard and Greenland, respectively. Such an increase in occurrence of NPF with

75 sea ice loss could be expected to increase CCN concentrations in the Arctic under future warmer conditions, though this is far from certain since changing sea ice extent is not the only controlling factor. Gilgen et al. (2018) found that reduction of sea ice in the year 2050 leads to increased emissions of DMS in a global aerosol-climate model. The increased DMS emissions, along with increased sea spray aerosol and meteorological changes, cause higher cloud drop number concentrations over the Arctic Ocean. This is in line with results from another global model study, Struthers et al. (2011), which used an atmospheric climate

80 model to investigate the response of sea spray aerosol to sea ice loss. They found a strong increase in sea salt emissions and thus higher cloud drop concentrations, but the effect on clouds and energy budget was uncertain due to poor model representations of aerosol-cloud interactions. In contrast to these studies, the results from Browse et al. (2014) suggest that interactions between aerosol particles of different sizes could lead to a suppression of NPF in an ice-free Arctic summer. Their results showed an increase in the sink of condensable vapours due to stronger emission of sea spray aerosol from the open water, resulting in a

85 decrease in the concentration of smaller particles from NPF. In addition, the growth of sea spray particles from condensation of vapours shifted the size distribution to larger sizes, leading to enhanced scavenging by precipitation and a decrease in drop concentrations.

The conflicting results from Browse et al. (2014), Gilgen et al. (2018) and Struthers et al. (2011) highlight the difficulty in modelling the Arctic aerosol budget and how it might change in future. Uncertainties in model parameterisations stem from the

90 knowledge gaps in processes controlling the aerosol budget, and cause differences in climate projections from different model

set-ups. For example, the sea spray parameterisations used in the Gilgen et al. (2018) and Struthers et al. (2011) studies include empirical representations of the effect of temperature on the sea spray aerosol size distribution, while the parameterisation used in the Browse et al. (2014) study does not. This could be a cause of the discrepancy in their predictions of sea spray aerosol response to sea ice loss, though this has not been studied. The studies also differ in their treatment of primary marine organic

95   emissions, with only the Browse et al. (2012) study including such a source. Some field studies from the Arctic have indicated the importance of primary marine organics in the region (Leck and Bigg, 2010; Karl et al., 2013), as well as raising questions about possible recycling mechanisms of particles after they are emitted (i.e. through ageing or the particle break-up theory, Lawler et al., 2021). The open questions surrounding primary marine emissions complicate modelling of Arctic NPF due to the the sink of condensable vapours from larger particles. Models with size-resolved aerosol microphysics and chemistry are

100 better equipped to study these questions than bulk, single-moment models considering total mass only.

Aitken mode particles can act as CCN in the Arctic, which increases the influence of NPF over the Arctic aerosol budget. Karlsson et al. (2022) used measurements of cloud residual particles (i.e. particles obtained by drying cloud droplets or ice crystals) from the high Arctic to show that Aitken mode particles were acting as CCN during a period of frequent boundary layer new particle formation. Observations of aerosol size distributions in and out of cloud in sub-Arctic Finland showed

105 that on average 30% of Aitken particles (defined as 25-95 nm) were activated to form droplets (Komppula et al., 2005). In Svalbard, measurements of cloud residuals (Karlsson et al., 2021) and cloud drop number concentrations (Koike et al., 2019) have been used to show the activation of particles smaller than 50 nm diameter during periods of high supersaturation, such as when updraft speeds are high or when accumulation mode concentrations are low. Results from parcel models and large-eddy simulation (LES) models are in agreement with the observations that Aitken particles can act as CCN (Pöhlker et al., 2021;

110 Bulatovic et al., 2021). Activation of Aitken particles means that particles formed by NPF and subsequent growth may only need to grow up 20-50 nm diameter to act as CCN in Arctic clouds, making it more plausible that such particles could survive long enough in the atmosphere to be important for cloud formation.

Recent observations from the high Arctic provide a new opportunity to explore the questions surrounding the source of summertime aerosol. The Arctic Ocean 2018 (AO2018) expedition took place in August and September 2018 between Sval-

115 bard and the North Pole (Vüllers et al., 2020). The observed properties and behaviour of the aerosol challenge our current understanding of aerosol sources and sinks. Firstly, mass spectrometry measurements clearly show that iodic acid is the main driver of NPF events, which occur primarily during sea ice freeze-up (Baccarini et al., 2020a). This process was not included in previous large-scale modelling studies. Secondly, the long time series of particle concentrations and size distributions provide an opportunity to understand how sources and sinks are related to the melting/freezing cycle and changes in photochemistry.

120 In particular, the observations show a distinct transition in aerosol behaviour in late summer, when the iodic acid NPF events begin to take place. Here we aim to interpret this change in behaviour in terms of changes in the dominant aerosol sources.

In this study we used measurements from AO2018 to evaluate the Arctic aerosol budget in the global climate model UKESM1. We compared the accuracy of simulations with NPF in the boundary layer to that of simulations with NPF in the free troposphere. We also introduced an iodic acid NPF scheme to the model to investigate iodic acid as an Arctic aerosol

125 source compared to other components of the Arctic aerosol budget. The observational datasets are introduced in Sect. 2. The
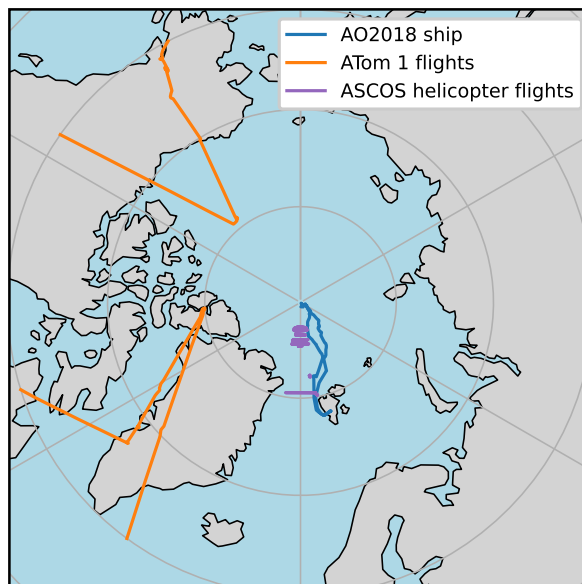
Figure 1. Map showing location of where observations where measured. Co-ordinates on map are for *Oden* during AO2018 (blue line), aircraft during leg 1 of ATom (orange line) and helicopter during ASCOS (pink line). Note only ATom 1 co-ordinates with a latitude greater than 60°N are shown here since we discarded data from further south in this study.

model is described in Sect. 3, including the different NPF schemes and our approach to the inclusion of iodic acid. Results are presented in Sect. 4 and discussed in Sect. 5.

2 Observations

We use data from three campaigns in different years: Arctic Ocean 2018 (AO2018), The Arctic Summer Cloud Ocean Study
130 (ASCOS) in 2008, and the Atmospheric Tomography Mission (ATom) in 2016. We only use model output from a simulation of the year 2018 because the Arctic Ocean 2018 dataset is the main focus of this study. The interannual variability in aerosol concentration may limit how representative observations from 2008 (ASCOS) or 2016 (ATom 1) can be to assess model output from 2018. However, as we will show in later sections, the difference in particle concentration from different simulations in this study can be several orders of magnitude and therefore is likely to exceed the range of concentrations that would be measured
135 in different years.

2.1 Arctic Ocean 2018

The Arctic Ocean 2018 (AO2018) expedition took place in August and September 2018 aboard the Swedish icebreaker *Oden*. The ship travelled from Svalbard to the North Pole and then drifted, moored to an ice floe, for 4 weeks before travelling back

to Svalbard (Fig. 1). Further details and meteorological conditions of the campaign are presented in Vüllers et al. (2020).
140 Here, we compare model output to aerosol and gas-phase measurements, which were measured during AO2018 as part of the Microbiology-Ocean-Cloud Coupling in the High Arctic (MOCCHA) campaign.

We use two aerosol datasets from the AO2018 campaign, involving three different instruments (Baccarini et al., 2020a). A differential mobility particle sizer (DMPS) measured particles in the size range 10–959 nm (Karlsson and Zieger, 2020). We integrate this size distribution over the ranges 15–100 nm and 100–500 nm. Total particle concentration for diameters greater
145 than 2.5 nm was measured by an ultrafine condensation particle counter (UCPC). The UCPC and integrated DMPS data were used to calculate the concentration of all particles in the size range 2.5–15 nm (Baccarini and Schmale, 2020). This 2.5–15 nm time series was also supplemented by a particle size magnifier during periods when the UCPC was not in operation. All data has been selected for "clean" periods, i.e. excluding periods where the ship's exhaust might influence the measurements. In addition to the aerosol data, iodic acid concentrations were measured using a nitrate chemical ionization mass spectrometer
150 (Baccarini et al., 2020b).

The measurements of nucleation mode particle concentration at the surface during AO2018 show marked difference in aerosol behaviour linked to the onset of local sea ice freeze-up. During the freeze period, peaks in the nucleation mode concentration occur during NPF events, lasting on the order of hours (see section 4.2). Thus the nucleation mode concentration is on average higher in the freeze period than the melt period, and also fluctuates more.

155 ## 2.2 Arctic Summer Cloud Ocean Study 2008

The Arctic Summer Cloud Ocean Study (ASCOS) campaign also took place on the icebreaker *Oden*, at roughly the same time of year as AO2018 but a decade earlier (2008). The ASCOS drift period was from 12th August until 2nd September 2008 and took place close to 87°N. A full description of the campaign is given in Tjernström et al. (2014).

A helicopter was used during ASCOS to take measurements above the surface, with two condensation particle counters
160 (CPCs) and one optical particle counter (OPC) used to measure aerosol concentrations. The CPCs and OPC detected particles larger than 3 nm, 14 nm, and 300 nm respectively, giving an overall aerosol size distribution in the ranges 3–14, 14–300 and >300 nm. These do not exactly match the aerosol size ranges available from the AO2018 data, but still give us valuable information about the aerosol size distribution from this campaign. The aerosol measurements are presented in Kupiszewski et al. (2013).

165 ## 2.3 Atmospheric Tomography Mission

The Atmospheric Tomography Mission (ATom) was a multi-year flight campaign that used the NASA DC-8 aircraft to study the effects of air pollution on the chemistry of the atmosphere. There were four legs of ATom, each carried out in a different season in different years. Here, we use measurements taken during the first leg, which took place in summer 2016. Measurements were taken over a wide range of latitudes and altitudes. We only use measurements taken north of 60°N.

170 Aerosol size distributions were measured during ATom using a nucleation-mode aerosol size spectrometer (NMASS), an ultra-high-sensitivity aerosol size spectrometer (UHSAS) and a laser aerosol spectrometer (LAS). The full set of ATom aerosol

measurements are presented in Brock et al. (2019). Aerosol size distributions are available for particles between approximately 3 nm and 3.5 μm diameters.

Note that the AO2018, ASCOS and ATom campaigns use instruments with different ways of sizing particles. The DMPS measures the electrical mobility diameter of particles. The CPCs and NMASS measure particles based on the critical diameter for droplet nucleation at the instrument's operating supersaturation. The OPC, UHSAS and LAS all rely on optical methods to measure particles, meaning they measure the optical equivalent diameter of particles. No attempt has been made to convert from optical equivalent diameter to mobility diameter. Such a conversion would require information about the refractive indices of the particles measured by the optical instruments, which is not available.

3 Model description

We used the UK Earth System Model version 1 (UKESM1, Mulcahy et al., 2020; Sellar et al., 2019) in its atmosphere-only configuration, which uses output from a fully-coupled run of UKESM1 to prescribe sea surface temperatures (SSTs) and some biogenic emissions, such as DMS, from the ocean. The dynamical core of the model is the UK Met Office Unified Model (UM) in global atmosphere configuration version 7.1 (GA7.1, Walters et al., 2019) with a horizontal resolution of 1.875° longitude by 1.25° latitude and 85 vertical levels. The vertical resolution is approximately 50 m at the surface, 150 m at 1 km altitude and on the order of km at the highest model level. We ran the model in its "nudged" configuration, which means horizontal winds and potential temperature are relaxed to ERA-Interim values on a 6-hourly time scale above approximately 1 km. The model simulates gas and aerosol chemistry using the UK chemistry and aerosols model (UKCA, Morgenstern et al., 2009; O'Connor et al., 2014). Aerosol microphysics is simulated by the Global Model of Aerosol Processes (GLOMAP-Mode, Mann et al., 2010) using 5 log-normal aerosol size modes (4 soluble and 1 insoluble). The model uses 2-moment aerosol microphysics, meaning that the number and mass in each mode are prognostic variables. There are four aerosol species: sulphate, organic carbon, black carbon and sea salt. Processes handled by GLOMAP include primary emissions, coagulation within and between modes, condensational growth and ageing, new particle formation, dry deposition, wet deposition within and below clouds, and aqueous sulphate production in cloud droplets.

Emissions of SO_2, black carbon (BC) and organic carbon (OC) are for the year 2014 for all emissions sectors except biomass burning, which are from a climatology of the years 1995-2004. We use a climatology for biomass burning to minimise any potential bias from boreal forest fire emissions not being from the same year as the simulation time. The emissions datasets used for aerosols and precursor vapours are Hoesly et al. (2018) (SO_2, anthropogenic OC and BC), Marle et al. (2017) (biomass burning OC and BC) and Sindelarova et al. (2014) (monoterpenes). Sea salt emissions are calculated using the Gong (2003) parameterisation. Primary marine organic emissions are then calculated using the sea spray flux, 10 m wind speed and chlorophyll-a concentration, using the Gantt et al. (2015) parameterisation. Note that because we use an atmosphere-only configuration in this study, the chlorophyll-a concentration is taken from an ancillary file, produced using model output from the fully-coupled model. Marine emissions are scaled by grid box open water fraction for sea ice regions.

3.1 New particle formation schemes

UKESM includes binary homogeneous nucleation of water and sulphuric acid (H_2SO_4) using the parameterisation of Vehkamäki et al. (2002). In this study, we included two additional NPF formation schemes in the model. We simulated nucleation of H_2SO_4 in the boundary layer (BL) by cluster activation as described by Kulmala et al. (2006) (hereafter K06). We simulated organically mediated H_2SO_4 nucleation using the parameterisation of Metzger et al. (2010) (hereafter M10). Simulations are labelled by their NPF scheme and the region of the atmosphere the scheme is applied to (e.g. BL for a scheme switched on in the boundary layer only or FT for a scheme switched on in the free troposphere only).

The formation rates of 1.5 nm clusters, J_*, used by M10 and K06 are given in cm^{-3} s^{-1} by

$$J_{*,K06} = k_{K06} C_{SA} \qquad (1)$$

$$J_{*,M10} = k_{M10} C_{SA} C_{secorg} \qquad (2)$$

where k_{K06} is 10^{-6} s^{-1}, k_{M10} is 10^{-13} cm^3 s^{-1}, and C_x are the concentrations of the precursor vapours in cm^{-3}. The 3 nm particle formation rate is calculated from the 1.5 nm cluster formation rates using the method from Kerminen and Kulmala (2002), which accounts for growth of clusters and loss to existing particles.

It should be noted that these two BL NPF schemes use empirical parameterisations that have not been developed with or tested against data from the Arctic. Moreover, the parameterisations only consider the influence of H_2SO_4 and secondary organic vapours. MSA and ammonia are not included in UKESM and thus are not modelled as NPF precursors in this study. These omissions are potential sources of bias given the importance of MSA and ammonia in the Arctic (Willis et al., 2018; Beck et al., 2020).

As we show below, entrainment of nucleation mode aerosol from the FT is an important process. To investigate the role of FT entrainment as a source of surface particles in the high Arctic, we ran an additional sensitivity test with an imposed NPF rate in the low FT (simulation M10_Prsc). A rate of 10^{-2} particles cm^{-3} s^{-1} was used for altitudes above the top of the BL and below 7.5 km, and for latitudes north of 80°N. Since this rate is higher than what the M10 scheme typically produces, it allows us to investigate the sensitivity of the surface concentrations to a strong free troposphere source.

3.2 Iodic acid

An empirical model for the steady-state concentration of iodic acid has been produced from observations taken in the high Arctic (Baccarini et al., 2020a). The concentration in cm^{-3}, C_{IA}, is given by

$$C_{IA} = \frac{E}{v_{dep} + h \cdot CS} \qquad (3)$$

where E is the emission rate of iodine atoms in cm^{-2} s^{-1}, v_{dep} is the dry deposition velocity of iodic acid in cm s^{-1}, h is the surface mixed layer height in cm and CS is the condensation sink due to existing aerosols, given in s^{-1}. It was observed

during AO2018 that fog and cloud droplets acted as a strong sink of the iodic acid, however we do not account for that here since the parameterisation of clouds in the coarse resolution model gridboxes is unlikely to be representative of conditions at
235   the ship.

We used Eq. (3) to diagnose the steady-state concentration of iodic acid in model gridboxes at each timestep. The iodic acid was then used as a precursor to drive NPF. The dry deposition velocity of iodic acid was calculated by the model assuming a diffusion constant equal to that of H_2SO_4. The condensation sink due to existing aerosols was calculated during model runs using the aerosol size distribution produced by the model. We use the modelled dry aerosol diameter in the condensation sink
240   calculation, meaning that the effects of water uptake by aerosol are not included. For the surface mixed layer height, we take the BL height calculated by the UM. Finally, we use a value of 5.21×10^6 cm^{-2} s^{-1} for E, which is approximately equal to the median of the distribution of E measured by Baccarini et al. (2020a).

The concentration of iodic acid was observed to increase towards the end of summer, during the sea ice freeze-up (Baccarini et al., 2020a). It is thought that the freezing of sea water can trigger the emission of iodine from the surface. To incorporate this
245   behaviour into UKESM, we calculate the concentration of iodic acid in gridboxes where sea ice fraction is non-zero and where the surface temperature is less than -5 °C. Although the observed freeze-up date is defined as the day when the 14-day running mean of surface temperature reaches -2 °C (the temperature at which sea water freezes), we found that -5 °C acted as a better threshold for ice freeze-up in the model. This is because there is a cold bias in the model such that when the observed 14-day running mean temperature reaches -2 °C, the modelled surface temperature is closer to -5 °C (see Fig. A1). The calculated
250   concentration of iodic acid is then equally distributed from the surface the BL height. This is equivalent to assuming that the lifetime of iodic acid is long enough for the gas to be mixed throughout the BL.

It is important to note that a direct/causal mechanism linking the freeze-up to enhanced iodine emissions has not yet been identified. However, the results of our study would remain valid even if the two processes were not directly related. In fact, the surface temperature threshold used in the model is a good tracer for the summer to autumn transition, which has been
255   associated with higher iodine concentration in the Arctic (Baccarini et al., 2020a; Sharma et al., 2019)

The particle formation rate at 3 nm from iodic acid is calculated using the method from Kerminen and Kulmala (2002) as for the H_2SO_4 activation and organically mediated schemes, using a kinetic rate of cluster formation from iodic acid. This is in line with recent results from cloud chamber experiments (He et al., 2021). The cluster formation rate in cm^{-3} s^{-1} is given by

$$J_{*,IA} = k_{IA} C_{IA}^2 \tag{4}$$

260   where $k_{IA} = 10^{-13}$ cm^3 s^{-1}. The mass created from HIO_3-driven new particle formation is added to the sulphate model component.

3.3   Secondary organic vapours

Assumptions about the production of secondary organic aerosol (SOA) material have a large effect on modelled Arctic aerosol. SOA is created in the model by the oxidation of monoterpenes by ozone, the hydroxyl radical and the nitrate radical (Spracklen

et al., 2006). These reactions produce SOA on the timescale of hours. This is a simplification of the process, since in reality there are many chemical species and reaction pathways involved in the production of SOA, which operate on a range of timescales and produce a range of volatilities. In particular, some SOA precursor species have a longer lifetime than monoterpene and can therefore be transported further in the atmosphere before forming SOA and condensing on existing aerosol. In the model, most monoterpene is oxidized close to the source region (e.g. boreal forests) and quickly condenses onto existing particles, therefore the concentration of SOA precursor gases is very low in the central Arctic; as a consequence, NPF involving organic vapours is extremely weak. To investigate the effect of these assumptions on Arctic NPF, we ran sensitivity simulations where the oxidation rate of monoterpene was reduced by a factor of 100. The labels of these simulations use the suffix _SecOrg.

3.4 Ageing of insoluble particles

The default assumptions in UKESM about particle ageing have a very substantial effect on Arctic aerosol, particularly where NPF is a major source of Aitken mode particles. Particle ageing in a model is the transfer of insoluble particles into the soluble particle modes after condensation of water-soluble material. In UKESM, sources of insoluble carbonaceous particles are biofuel and biomass burning emissions (mean diameter 150 nm), fossil fuel burning emissions (mean diameter 60 nm) and primary marine organic carbon emissions (mean diameter 160 nm). By default, the aged mass from the insoluble mode is moved into the soluble Aitken mode (Mulcahy et al., 2020). However, the mean diameter of the insoluble mode does not usually correspond to the size limits of the soluble Aitken mode, and this can lead to undesirable behaviour in the model. Thus, when mass from the insoluble mode is moved into the soluble Aitken mode, it will typically increase the mean diameter of the soluble mode beyond its upper limit (100 nm). When small particles enter the Aitken mode following growth of nucleation mode particles, they are artificially strongly depleted because "mode merging" (Mann et al., 2010) requires that their mass is averaged with the larger particles already existing in the Aitken mode. This combination of assumptions (the size of aged particles and mode merging) is adequate for reproducing size distributions in the mid-latitudes, where anthropogenic and fire emissions are a more dominant source. However, our early simulations showed that this method has a very substantial effect in the Arctic where NPF is occurring in air that has aged during long-range transport from low latitudes to the Arctic (see appendix B). In particular, we found that the particle size distribution was extremely insensitive to the NPF rate. We therefore altered the model such that aged carbonaceous particles are moved directly into the soluble accumulation mode (100 – 500 nm), as is appropriate for their diameter. Our CONTROL simulation uses this altered ageing scheme. Simulations using the model's default ageing scheme are presented in appendix B.

A description of all model simulations is given in Table 1.

4 Results

We organise the results as follows. First we examine the behaviour of our empirical iodic acid scheme by comparing modelled surface iodic acid concentrations to observations in Sect. 4.1. Then in Sect. 4.2 we consider the effect of different BL NPF schemes in the model (including iodic acid) on the surface aerosol concentration during AO2018. Since we show that BL NPF

Table 1. Description of simulations.

Simulation	Description
CONTROL	Model set-up based on UKESM1 atmosphere-only configuration. Binary H_2SO_4-water vapour NPF parameterised as per Vehkamäki et al. (2002).
K06_BL	Additional BL H_2SO_4 NPF parameterised by Kulmala et al. (2006)
M10_ALL	Organically-mediated NPF in all model levels, using Metzger et al. (2010)
M10_BL	Organically-mediated NPF in the BL, using Metzger et al. (2010)
M10_Prsc	As M10_ALL, but with a prescribed NPF rate of 10^{-2} cm^{-3} s^{-1} between the BL top and 7.5 km and north of 80°N
IA_BL	Additional BL NPF driven by IA
IA_BL_M10_ALL	As M10_All but with additional BL NPF driven by IA
M10_BL_85N	Additional NPF in the BL using Metzger et al. (2010) for gridboxes north of 85 °N only
XXX_SecOrg	Additional change to oxidation of monoterpenes as described in section 3.3

is not taking place locally during the melt period of AO2018, we consider FT NPF as a source of surface particles in Sect. 4.3, using surface observations from AO2018 and aerosol profiles from ASCOS in 2008 and ATom in 2016. Finally, we consider a combination of local (BL) and non-local (FT) NPF in Sect. 4.4.

300   When comparing model output to observations of surface aerosol concentration, we use the overlap index defined in Pastore and Calcagnì (2019) to quantify the similarity between the distribution in aerosol concentration from observations and different model simulations. An overlap index of 0 indicates no overlap between the distributions, while an overlap index of 1 indicates that the two distributions are identical. Overlap indices closer to 1 therefore indicate simulations with good model-observation agreement in terms of the magnitude and variability of the two time series even if individual peaks and troughs do not match
305   temporally.

4.1   Iodic acid concentration

Figure 2 shows a time series and PDF of surface HIO_3 concentration from observations and model output. To colocate the model output with the ship, we take the model gridbox nearest the ship's position. In the observations, the surface HIO_3 concentration is lower in the melt period (before day 239) than in the freeze period (after day 239). The surface concentration
310   in the freeze period has a baseline of approximately 10^6 cm^{-3} and peak values 5–6 times higher lasting on the order of hours, whereas in the melt period the concentration reaches 10^6 cm^{-3} only for brief periods, such as on day 228. The periods of peak surface concentration in the freeze period correspond to observed NPF events.

In the model, HIO_3 is only emitted when the surface temperature is -5 °C or less. The modelled temperature reaches this threshold on approximately day 236 at the ship's position, such that the model starts to emit HIO_3 at a similar time to the
315   observed freeze-up onset (day 239), when HIO_3 concentrations were observed to increase at the ship. After HIO_3 starts to be emitted in the model, the empirical scheme we use for HIO_3 production consistently calculates surface HIO_3 concentration to
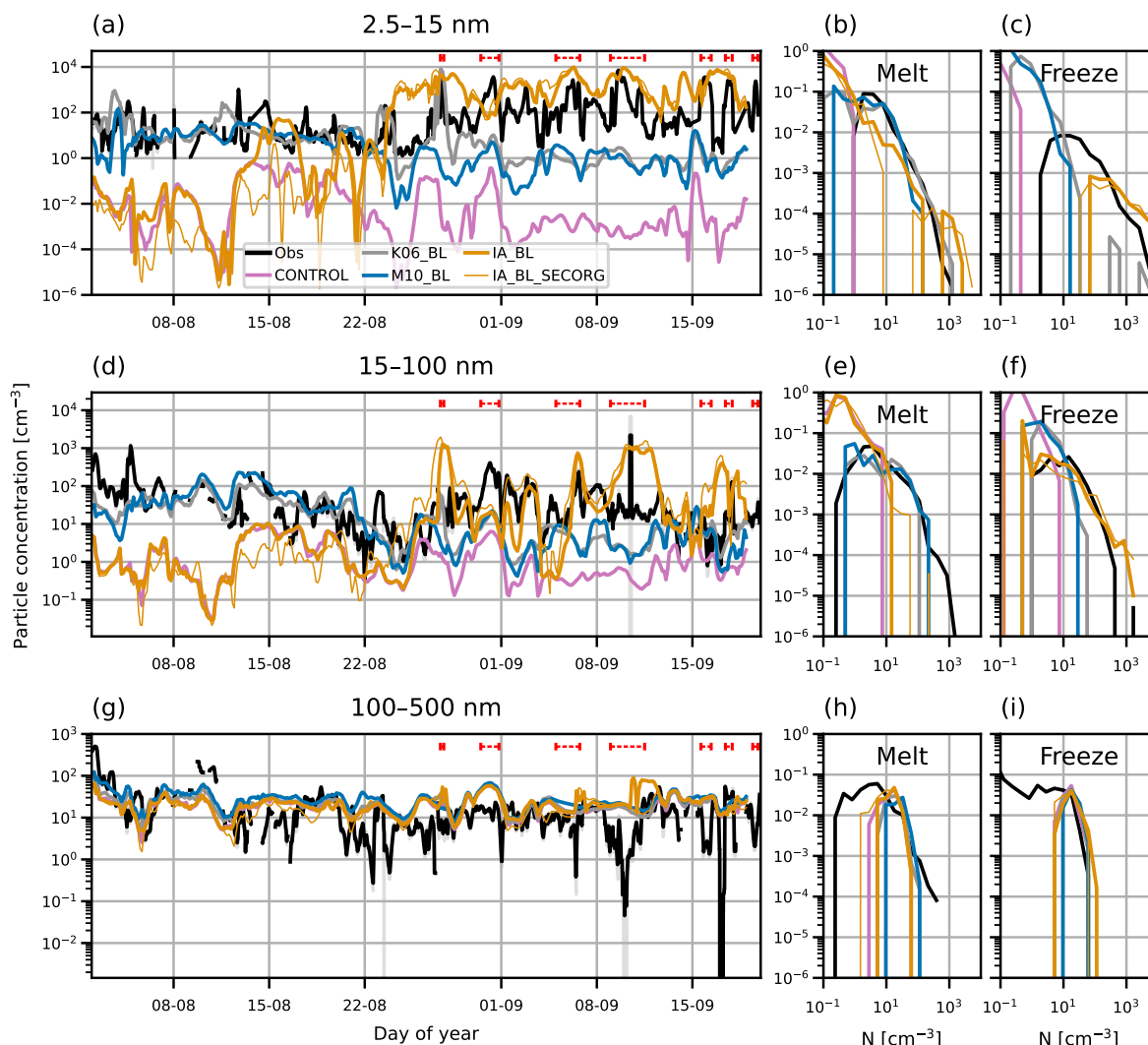
Figure 2. Times series and PDF of surface iodic acid concentration during AO2018 from observations and model output. Model output is from simulation IA_BL (orange lines). Observations are shown as 3-hourly mean (black lines). Red dashed lines in (a) show periods of observed NPF events. PDF of concentration is for freeze season only, i.e. after 27th August 2018 (day 239).

be the same order of magnitude as the observations. The PDF in Fig. 2(b) is for the freeze season only, i.e. day 239 onward. The observed distribution of surface HIO_3 concentration is broadly captured, though the model does not reproduce the highest or lowest observed concentrations. This is likely to be because the model does not resolve the spatially heterogeneous sea ice

320   state (which controls the emissions of iodic acid) nor the variability in clouds and fog, which control iodic acid scavenging as well as influencing the condensation sink due to existing aerosols.
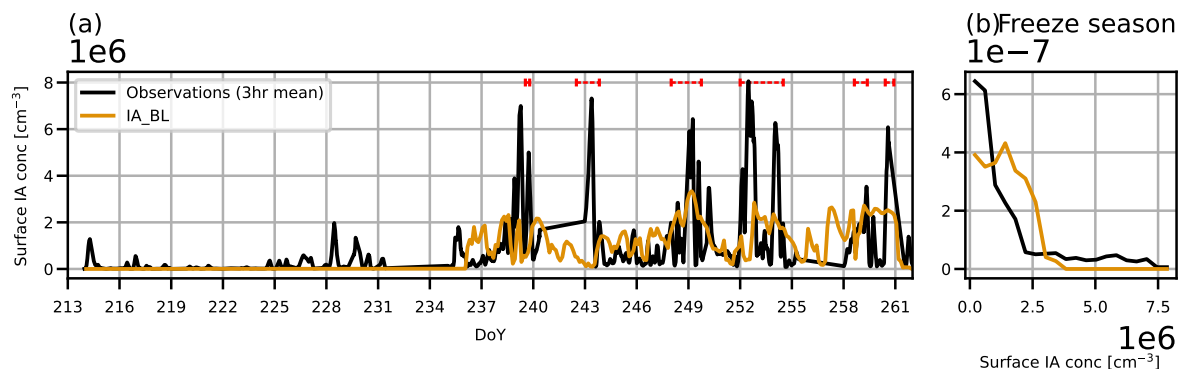
Figure 3. Times series and PDFs of surface aerosol concentration during AO2018 from observations and model simulations with various boundary layer NPF mechanisms. Model output is from simulations CONTROL (pink lines), K06_BL (grey lines), M10_BL (blue lines), IA_BL (thick orange lines) and IA_BL_SecOrg (thin orange lines). Observations are shown as 3-hourly mean (black lines) and standard deviation (grey shading). Aerosol concentrations are shown for particles with diameter (a-c) 2.5-15 nm, (d-f) 15-100 nm and (g-i) 100-500 nm. Red dashed lines in (a, d, g) show observed NPF events. PDFs are separated by observed sea ice freeze-up date, 27th August 2018 (day 239).

4.2 Effect of NPF in the boundary layer

4.2.1 Time series of particle concentrations

Figure 3 shows time series and PDFs of surface aerosol concentration in three particle size ranges from the AO2018 ob-
325 servations and for simulations CONTROL, K06_BL, M10_BL, IA_BL and IA_BL_SecOrg. Observations are from the ship (approximately 15 m above the ground) and model output is for the first model level, between approximately 0 and 37 m.

A time series of the measured nucleation mode (2.5–15 nm diameter) particle concentration during AO2018 is shown in Fig. 3 (a). Periods where iodic acid NPF events were observed are marked with red dashed lines. There is a marked difference in the behaviour of the nucleation mode concentration before and after the onset of sea ice freeze-up (27th August 2018, day 239).
330 In the melt period (up to day 239), the nucleation particle concentration rarely exceeds 100 cm^{-3} and is usually between 1–10 cm^{-3}. The NPF events, which occurred after the freeze-up began in the vicinity of the ship on day 239, are associated with peaks in the nucleation mode particle concentration lasting a few hours, causing fluctuations in particle concentration between approximately 10 and 10^4 cm^{-3}, consistent with a strong local source.

The modelled nucleation mode particle concentration is underestimated in simulations CONTROL, IA_BL and IA_BL_SecOrg
335 in the melt period, while the inclusion of HIO$_3$ NPF means that IA_BL and IA_BL_SecOrg perform better in the freeze period than during the melt. The nucleation mode concentration in CONTROL varies from roughly 10^{-6} to 10^{-1} cm^{-3} and is usually at least an order of magnitude lower than observed throughout the whole period. In contrast, simulations with HIO$_3$ (IA_BL and IA_BL_SecOrg) produce nucleation mode concentrations of roughly the correct order of magnitude during the

Table 2. Overlap indices calculated for the PDFs of nucleation, Aitken and accumulation aerosol concentrations from observations and each simulation, measured at the surface. PDFs are separated into the melt and freeze periods before overlap indices are calculated. Bold text indicates the greatest overlap index in each mode for the melt and freeze periods.

Simulation	Nucleation		Aitken		Accumulation	
	Melt	Freeze	Melt	Freeze	Melt	Freeze
CONTROL	0.01	0.00	0.31	0.12	0.57	0.64
K06_BL	**0.75**	0.12	0.72	0.31	0.53	0.63
M10_ALL	0.72	0.06	0.71	0.40	0.52	0.55
M10_ALL_SecOrg	0.66	0.26	0.61	0.60	0.56	0.55
M10_BL	0.73	0.05	0.73	0.34	0.50	0.55
M10_BL_85N	0.01	0.00	0.33	0.13	0.56	0.67
M10_Prsc	0.35	0.52	**0.75**	0.37	0.51	0.55
M10_Prsc_SecOrg	0.20	**0.61**	0.64	0.66	0.57	0.55
IA_BL	0.25	0.47	0.35	0.70	0.58	0.58
IA_BL_SecOrg	0.13	0.40	0.30	0.59	**0.65**	**0.69**
IA_BL_M10_ALL	0.63	0.51	0.69	**0.77**	0.55	0.56

freeze period (day 239 onwards), with a distinct change in concentration and behaviour around day 235. However, the lack of
340 HIO$_3$ emissions during the melt period means that the model continues to underestimate the concentration by several orders of magnitude. The model underprediction of nucleation mode particle concentration in the melt period is an indication that HIO$_3$ NPF is not the only part of the regional aerosol budget that needs consideration to produce an accurate simulation. Simulations K06_BL and M10_BL both use BL NPF schemes and have higher nucleation mode concentrations than CONTROL as a result. In the melt period, K06_BL and M10_BL both consistently simulate nucleation mode concentrations of the same order of
345 magnitude as the observations. Interestingly, the two simulations have very similar nucleation mode concentrations despite the differences in the NPF schemes. K06_BL occasionally simulates higher nucleation mode concentrations than M10_BL, most notably on days 239–243. In the freeze period, K06_BL and M10_BL still underestimate the nucleation mode concentration despite simulating higher concentrations than CONTROL.

Overlap indices for the PDFs of observed surface aerosol concentration and modelled concentration from all simulations are
350 given in Table 2. The underestimation of nucleation mode concentration by simulation CONTROL is highlighted by the fact that its overlap indices are close to 0 in both the melt and the freeze periods. The K06_BL and M10_BL PDFs of nucleation mode concentration for the melt period match the observations well, producing overlap indices of 0.73 for M10_BL and 0.75 for K06_BL, which is the highest value achieved for the nucleation mode in the melt period. In the freeze period, the overlap indices are also low (0.05 for M10_BL and 0.12 for K06_BL).
355 Observed Aitken mode concentrations (diameter 15–100 nm) lie between about 1 and 1000 cm^{-3}, with a a mean of 60 cm^{-3} over the whole period. In contrast, concentrations in the CONTROL simulation are around 1 cm^{-3}, frequently fall

below 0.1 cm^{-3}, and never exceed 10 cm^{-3}. The simulations with HIO$_3$ again show a sharp increase in particle concentration around day 235 when HIO$_3$ starts being emitted during the freeze period. Model Aitken mode concentrations then vary between being comparable to the observations and being 1–2 orders of magnitude too low. The Aitken mode concentration in simulation
360   IA_BL_SecOrg behaves similarly to that of IA_BL, although there are some periods where the concentration in IA_BL_SecOrg exceeds those in the IA_BL simulation by a factor of more than 10 and is in better agreement with observed concentrations (notably days 244–247). This is likely because of the extra condensable vapour in IA_BL_SecOrg, which promotes more particle growth from the nucleation mode. As in the nucleation mode, the Aitken mode concentrations from K06_BL and M10_BL are higher than CONTROL, on the same order of magnitude as the observations in the melt period but underestimating
365   observations in the freeze period.

The observed accumulation mode concentrations (diameter 100–500 nm) are typically around 10–100 cm^{-3}, with brief periods of less than a day where they fall to 1 cm^{-3} or lower, which is characteristic of the central Arctic (Bigg et al., 1996; Bigg and Leck, 2001; Mauritsen et al., 2011; Leck and Svensson, 2015). All simulations capture the observations well, except for the periods of extremely low concentration. The good agreement shows that NPF is not an important source of accumulation mode
370   aerosol. As shown in e.g. Stevens et al. (2018) and Loewe et al. (2017), the periods of very low concentration are associated with efficient scavenging in drizzle on smaller spatial scales than represented in a global model. Nevertheless, the generally good model-observation agreement means that the aerosol surface area, and hence condensation sink for nucleating vapours, is reasonable in the model, and therefore not a cause of the biases in nucleation and Aitken mode particle concentrations.

4.2.2   Aerosol vertical profiles

375   In Sect. 4.2.1, we showed that the use of BL NPF schemes (instead of only the default upper tropospheric scheme) increased nucleation and Aitken particle concentrations at the surface during the melt period of AO2018. In this section, we examine the effect of these schemes on particle concentrations aloft.

Figure 4 shows simulated nucleation mode aerosol vertical profiles for the AO2018 campaign period. As discussed in Sect. 4.2.1, the nucleation mode concentrations at the surface in CONTROL are typically less than 0.1 cm^{-3} and never above 1
380   cm^{-3}. We showed that this is an underestimation of the measurements taken at the ship. Figure 4 shows that despite the low concentrations at the surface, the model produces nucleation mode concentrations of up to 1000 cm^{-3} in the low FT, for example on day 244 above approximately 4 km. These higher concentrations aloft suggest that NPF is being simulated in the FT, but that those particles do not reach the surface.

The vertical profile for simulation M10_BL shows that the nucleation mode concentration is higher than CONTROL above
385   the BL as well as at the surface, even though this simulation is using the same NPF mechanism as CONTROL in the FT. We previously showed that M10_BL had nucleation mode concentrations at the surface that were 1–3 orders of magnitude higher than that of CONTROL. In the FT, the increase is up to an order of magnitude. The white lines in Fig. 4 show the modelled BL height, which is used by the NPF schemes to separate the BL from the FT. The increased nucleation mode concentrations in M10_BL above this BL height suggest that particles are being created in the BL at lower latitudes and then transported north
390   in the FT. To examine this effect further, we ran a simulation where the M10 scheme was used in the BL only for latitudes
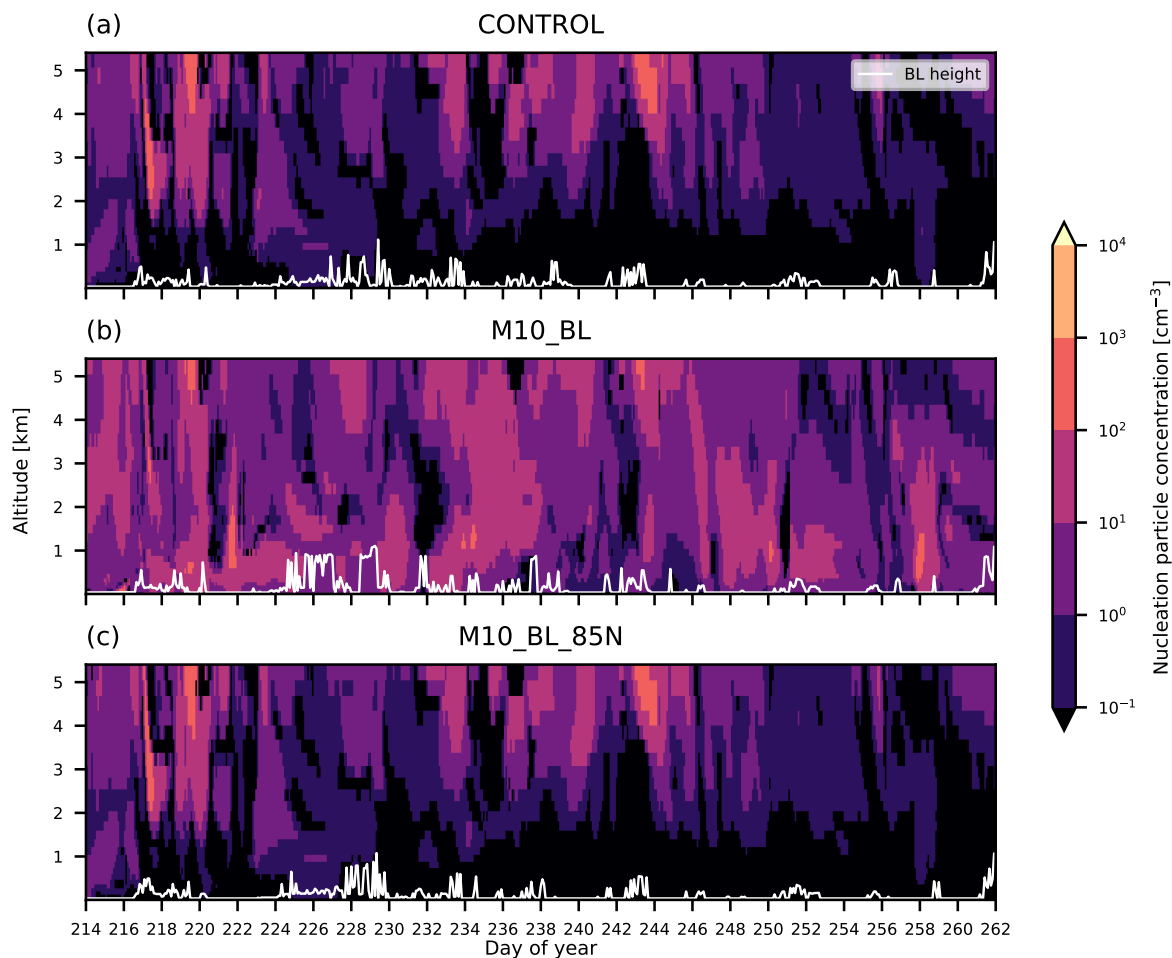
Figure 4. Nucleation mode aerosol profiles simulated for AO2018 campaign period. Model output is from simulations (a) CONTROL, (b) M10_BL and (c) M10_BL_85N. Model output was colocated with the position of the *Oden*. White lines show BL height.

north of 85°. The nucleation mode vertical profile for this simulation, M10_BL_85N, is also shown in Fig. 4 and shows lower concentrations than M10_BL in both the BL and the FT. In fact, the nucleation mode concentration in M10_BL_85N is mostly the same as that of CONTROL. The output from M10_BL_85N therefore shows that the higher concentrations in M10_BL are from latitudes south of 85°. The concentration of organic vapours north of 85°N is much lower than at lower latitudes (see the steep latitudinal gradient in Fig. D2), which potentially accounts for the low particle concentrations in M10_BL_85N. Note that the smaller spatial extent of the NPF scheme could lead to less depletion of precursors than when the scheme is used globally, thereby increasing the NPF rate in M10_BL_85N relative to M10_BL. However, this non-linear behaviour would have the opposite effect to what we describe here so we can disregard it.

4.3 Effect of free-tropospheric NPF

400 In Sect. 4.2 we showed that the model default NPF scheme is insufficient to produce an accurate simulation of the aerosol concentrations measured at the surface during AO2018. The inclusion of iodic acid NPF improves the concentration in the nucleation and Aitken modes in the freeze period. Nevertheless, substantial model underestimations in particle concentration remain during the melt period, indicating some other missing source. Simulations with BL NPF driven by H_2SO_4 or a combination of H_2SO_4 and secondary organic vapours produce more accurate surface concentrations in the melt period of AO2018

405 compared to observations. However, as we showed in Sect. 4.2.2, these simulations do not produce more NPF in the BL in the high Arctic. Rather, small particles produced at lower latitudes are transported north, increasing nucleation and Aitken concentrations aloft as well as at the surface. This behaviour in the model suggests that the FT could be a source of particles to the surface, either from particles created by NPF aloft, or in the BL at lower latitudes before being transported into the high Arctic FT. Such a source has been considered before, for example by Korhonen et al. (2008a), who showed that entrainment

410 of secondary particles from the FT is an important source of CCN over the Southern Ocean in GLOMAP, and **?** who used a high resolution LES model to show that particles can be transported from the free troposphere to the surface under conditions typical of the high Arctic. Also of relevance to entrainment processes in Arctic clouds, Solomon et al. (2011) used an LES model to show that a humidity inversion and entrainment of water vapour at cloud top helps to maintain the cloud by supplying moisture.

415 In this section we explore the role of the FT as a source of particles at the surface in both periods. We ran a simulation with M10 switched on at all model levels. We also ran a simulation with a fixed NPF rate for model levels between the top of the BL and 7.5 km.

4.3.1 Aerosol vertical profiles

Figure 5 compares simulated aerosol vertical profiles against observations from ASCOS (see Sect. 2.2). Model particle concen-

420 trations in these size ranges were calculated using August 2018 monthly mean data, colocated with the ASCOS flights which took place in August 2008. Concentrations of 3–14 nm diameter particles were consistently in the range 10^2–10^3 cm^{-3} in the FT, with lower values recorded below 1 km. The CONTROL simulation fails to capture these concentrations, underestimating the ASCOS mean concentration throughout the profile by 2 orders of magnitude in the FT and 3 orders of magnitude at the surface. Inclusion of organic NPF (M10_ALL) substantially increases particle concentrations, but they remain at least 1 order

425 of magnitude lower than observed. Even when we allow much higher concentrations of organic vapours to be transported into the Arctic (M10_ALL_SecOrg), 3–14 nm diameter particle concentration is still underestimated by up to 1 order of magnitude throughout the profile. The model captures the 14–300 nm concentration better than the smaller particles. This is consistent with the results from the AO2018 comparisons, where the accumulation mode was captured much better than the nucleation or Aitken modes. All simulations shown here have 14–300 nm diameter particle concentrations of the same order as those

430 measured in the ASCOS flights.
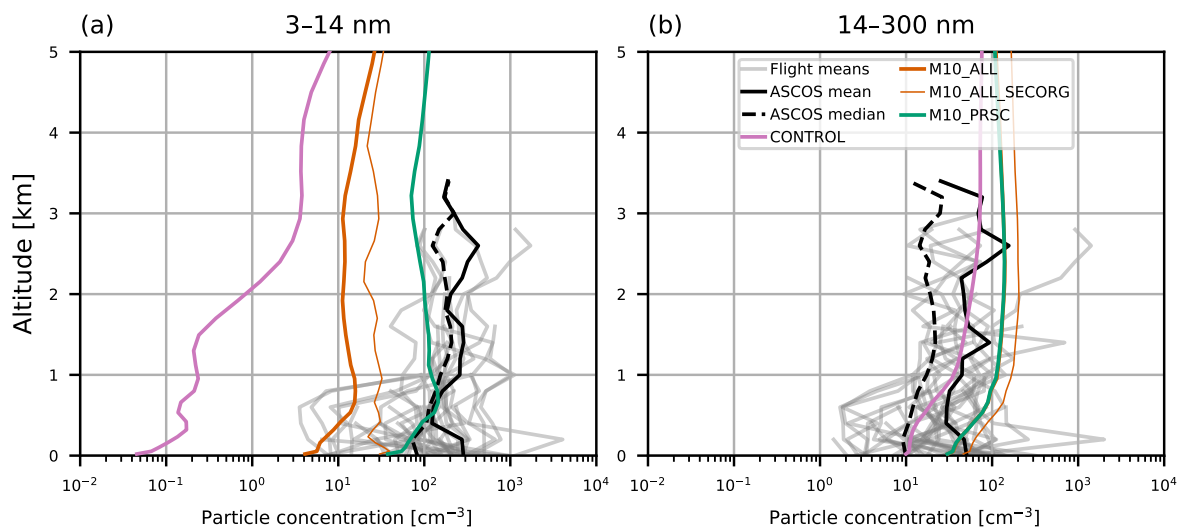
Figure 5. Aerosol vertical profiles from model output and ASCOS campaign observations from 2008. Model output is from colocated 2018 monthly mean values from simulations CONTROL (pink), M10_ALL (thick orange lines), M10_ALL_SecOrg (thin orange lines) and M10_Prsc (dark green). Observed values are given as the mean profile from each ASCOS flight (grey lines), overall mean (solid black) and overall median (dashed black). Profiles are for particles with size (a) 3-14 nm, measured during ASCOS using a UCPC and (b) 14-300 nm, measured using a CPC (particles greater than 14 nm) and a CLASP instrument (particles greater than 300 nm).

Aerosol vertical profiles measured in 2016 during the ATom campaign are shown in Fig. 6 with model output for the year 2018. Consistent with the ASCOS and AO2018 datasets, the CONTROL simulation predicts 5–10 nm diameter particle concentrations up to 3 orders of magnitude lower than the ATom measurements in the lowest 5 km of the atmosphere, with the largest model-observations discrepancies at the surface. In contrast to ASCOS, the M10_ALL simulations captures the

435 nucleation mode profile better, producing concentrations that are within the range of the ATom measurements. The Aitken mode is underestimated by all simulations, though simulation M10_ALL is closer to the observations than CONTROL in the lowest part of the FT. All simulations capture the accumulation mode well at the surface but underestimate particle number aloft by roughly 50%.

M10_ALL underpredicts the profile of nucleation mode aerosol measured during the ASCOS campaign, even after per-

440 turbing the model monoterpenes to increase the availability of precursors in the Arctic (M10_ALL_SecOrg). We therefore artificially tested what NPF rate would be required to explain these observed profiles. We tested various prescribed nucleation rates applied above the boundary layer. A rate of 10^{-2} cm^{-3} s^{-1} produced a nucleation mode profile in best agreement with ASCOS and ATom (M10_Prsc). In the ASCOS region (the central Arctic), M10_Prsc is the only simulation to produce 3–14 nm particle concentrations close to the observed profiles (Fig. 5). In the ATom region over continental North America,

445 M10_ALL and M10_Prsc both behave the same. We prescribed the nucleation rate in the model for latitudes north of 80 °N,
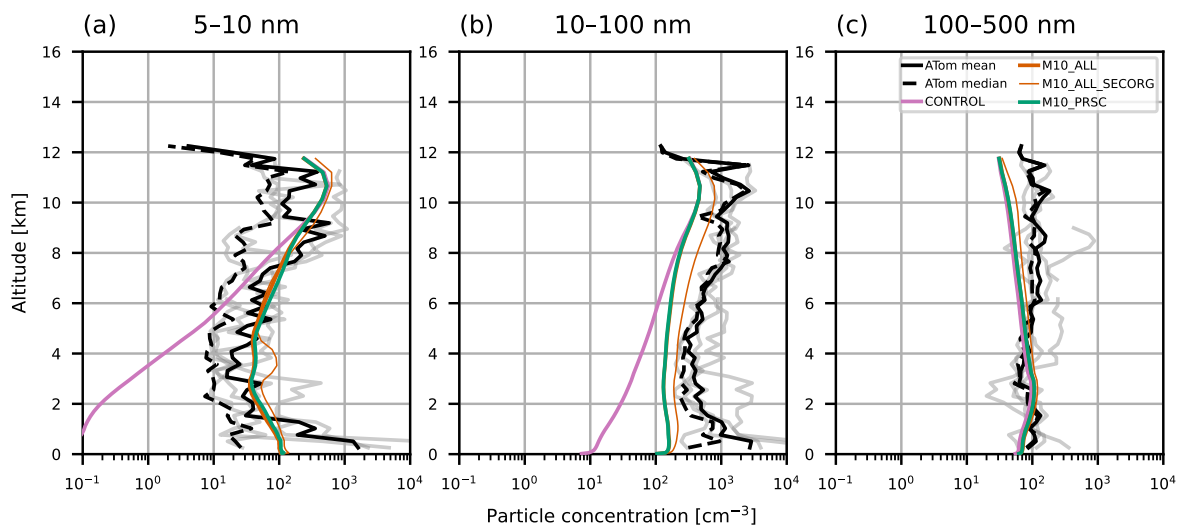
Figure 6. Aerosol vertical profiles from model output and ATom campaign observations from 2016. Model output is from colocated 2018 monthly mean values from simulations CONTROL (pink), M10_ALL (thick orange lines), M10_ALL_SecOrg (thin orange lines) and M10_Prsc (dark green). ATom observations are taken from leg 1 of the campaign and restricted to measurements that were taken north of 60°N. Observations correspond to mean profiles from different days (grey lines), the overall mean (black solid lines) and overall median (black dashed lines). Profiles are for particles with size (a) 5–10 nm, (b) 10–100 nm and (c) 100–500 nm. Observations were recorded at standard temperature and pressure, model output has been adjusted to account for this.

which means it has little effect over the ATom area. We also tested the prescribed rate in gridboxes north of 60 °N and still found good agreement with the ATom and ASCOS profiles (Figs. C1 and C2).

The model output shown in Figs. 5 and 6 is for the year 2018, while the obervational data is from 2008 (ASCOS) and 2016 (ATom). However, the large underestimations of the nucleation mode by simulation CONTROL (up to 3 orders of magnitude
450   at the surface) for both campaigns is unlikely to be because of interannual variability alone. The CONTROL simulation also underestimates the particle concentrations from the AO2018 campaign, which was in the same year as our model output.

4.3.2   Time series of particle concentrations

Time series and PDFs of particle number concentration at the surface from AO2018 observations and simulations M10_ALL and M10_Prsc are shown in Fig. 7 for nucleation, Aitken and accumulation mode particles.
455   In the nucleation mode, simulations M10_ALL and M10_Prsc both increase the simulated particle concentration by 2–3 orders of magnitude in the melt period relative to CONTROL (Fig. 2). Like M10_BL, M10_ALL captures the observed nucleation mode concentration well in the melt period. The higher FT NPF rate in M10_Prsc produces a nucleation mode concentration that is 1–2 orders of magnitude higher than M10_ALL. This higher concentration in M10_Prsc further demonstrates the way the FT is acting as a source of particles to the surface in the model, although the fixed NPF rate in M10_Prsc overestimates
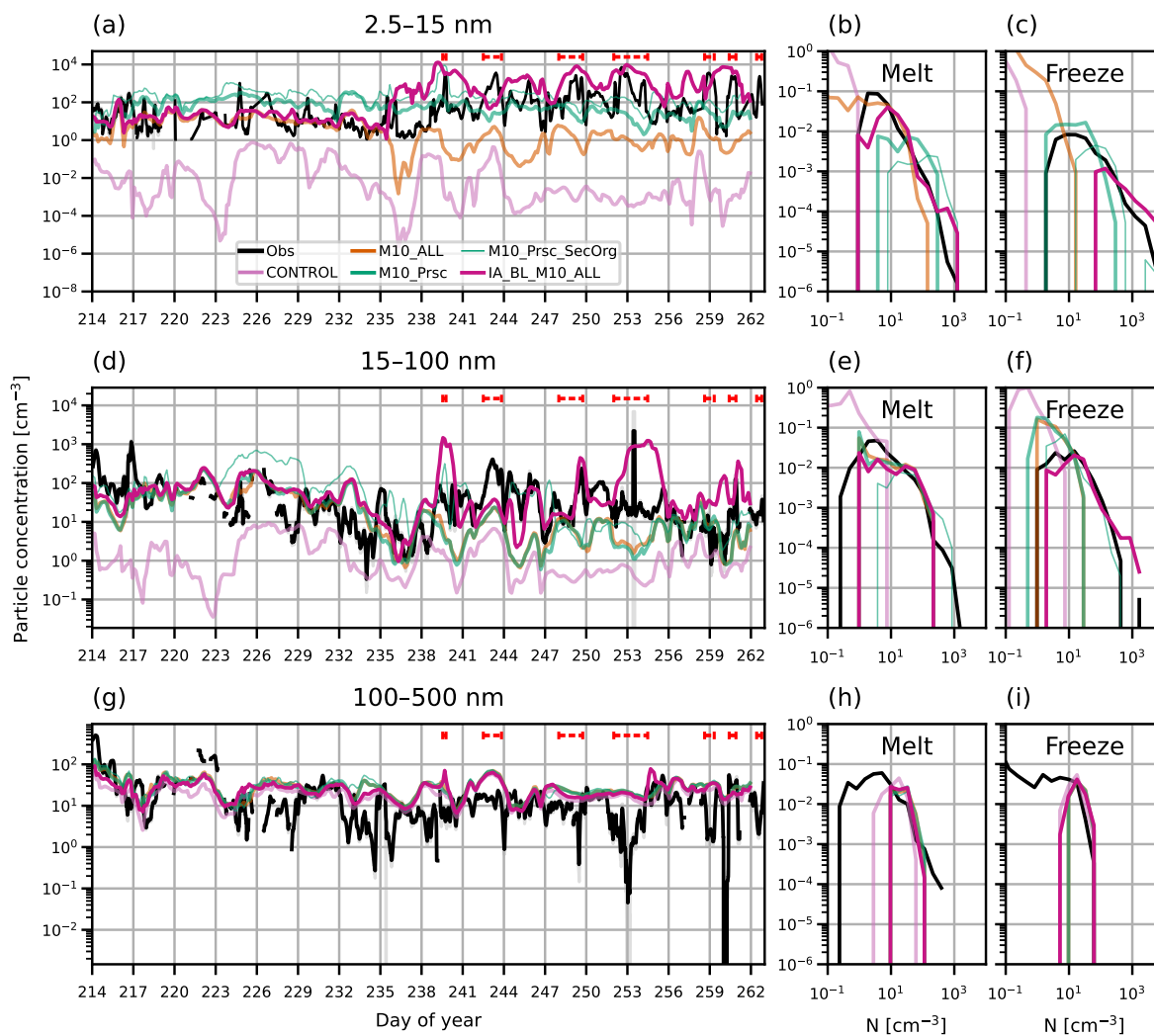
Figure 7. Time series and PDFs of aerosol concentration at the surface during AO2018 from observations and model output. Model output is from simulations M10_ALL (orange lines), M10_Prsc (thick green lines), M10_Prsc_SecOrg (thin green lines) and IA_BL_M10_ALL (red lines) Other than IA_BL_M10_ALL and the observations, lines have been made slightly transparent on this figure so that it is easier to view the results from IA_BL_M10_ALL. Observations are shown as 3-hourly mean (black lines) and standard deviation (grey shading). Aerosol concentrations are shown for particles with diameter (a–c) 2.5–15 nm, (d–f) 15–100 nm and (g–i) 100–500 nm. Red dashed lines in (a, d, g) show observed NPF events. PDFs are separated by observed sea ice freeze-up date, 27th August 2018 (day 239).

460   the nucleation mode concentration in the melt period. The nucleation mode concentration declines from the melt to the freeze period in M10_ALL. The particle concentration decreases from above 1 cm^{-3} in the melt period to approximately 1 cm^{-3}, occasionally reaching 0.1 cm^{-3}. M10_Prsc produces concentrations close to 100 cm^{-3} in the both periods. As such, M10_Prsc

1https://doi.org/10.5194/egusphere-2022-1079

captures the lower end of the observed distribution of nucleation concentration in the freeze periods, but does not capture the highest concentrations seen during the NPF events.

465   In the Aitken mode, particle concentrations are also higher in M10_ALL and M10_Prsc than in CONTROL. Despite differences between M10_ALL and M10_Prsc in the nucleation mode, they produce the same concentration of Aitken particles. Melt-period Aitken particle concentrations in M10_ALL and M10_Prsc are 1–3 orders of magnitude higher than in CONTROL, taking them to within 1 order of magnitude of the observed particle concentration for most of the melt period. As in the nucleation mode, Aitken concentrations decrease in M10_ALL and M10_Prsc in the freeze period such that the observations

470   are underestimated by 1–2 orders of magnitude in the freeze period. The declining Aitken concentrations in both of these simulations suggests a decrease in the particle growth rates towards late summer, possibly driven by declining photochemical production of precursor vapours (see appendix D). The Aitken mode concentration decreases even in M10_Prsc, which has a fixed NPF rate above the BL, highlighting that particle growth by condensation is an important process as well as the particle formation rate itself.

475   The accumulation mode is well captured by both M10_ALL and M10_Prsc. As for IA_BL, the changes to the model NPF scheme in the M10 simulations have little effect on the accumulation mode concentration relative to CONTROL.

Local formation processes in M10_Prsc are dominated by the fixed nucleation rate above the BL. However, local particle formation is also affected by the availability of condensable vapours (if new particles grow faster, they are more likely to survive in the atmosphere for longer rather than being lost to coagulation with other particles). Therefore, since growth is important,

480   we tested the sensitivity of NPF in the M10_Prsc simulation to the availability of secondary organic vapour by allowing more vapour to be transported to the Arctic in simulation M10_Prsc_SecOrg. Time series and PDFs of surface particle concentration during AO2018 is shown on Fig. 7. In the nucleation mode, M10_Prsc_SecOrg produces a concentration of approximately 100 cm^{-3}, behaving similarly to M10_Prsc.

In the Aitken mode, there are periods where M10_Prsc_SecOrg behaves the same as M10_Prsc and brief periods where it

485   produces higher concentrations. For example, on days 223–229, the concentration in M10_Prsc_SecOrg is nearly an order of magnitude greater than that from M10_Prsc, resulting in an overestimation of the observed Aitken concentration.

4.4   Combining local and non-local NPF

Overall, M10_ALL performs well in the melt period of AO2018 but still underestimates particle concentration in the freeze period. This suggests that a combination of secondary particles from aloft and local BL NPF involving iodic acid is re-

490   quired to capture the full aerosol time series. The combined simulation of M10_ALL and IA_BL is shown as simulation IA_BL_M10_ALL in Fig. 7. IA_BL_M10_ALL captures both the baseline of the nucleation mode in the melt period and the peaks in the freeze period. In the Aitken mode, IA_BL_M10_ALL is within 1 order of magnitude of the observations except for a few brief periods, such as days 253–255 when the observed concentration is overestimated in the model.

The behaviour of the simulations can be summarised by comparing the overlap of PDFs of simulated particle concentration

495   with those from observations (Table 2). Simulations with H_2SO_4 or organically-mediated NPF in the BL (K06_BL, M10_BL, M10_ALL, IA_BL_M10_ALL) have higher overlap indices for the nucleation and Aitken modes than CONTROL in the melt

Vapour species	Change in concentration from Aug to Sep 2018 [%]
DMS	-28.8
SO_2	135.2
H_2SO_4	-85.2
OH	-87.7
Monoterpenes	31.2
Secondary organics	-5.9

Table 3. Table of change in simulated concentrations of different vapours from August to September 2018 in simulation CONTROL. Concentration changes are given as the change in the mean value over gridboxes at the surface with latitude 80–90 N.

period, when the source of secondary particles from the FT has the greatest influence, but lower indices in the freeze period. During freeze-up, IA_BL_M10_ALL slightly overestimates the nucleation mode concentration, meaning that its nucleation mode overlap index in this period (0.51) is lower than that of M10_Prsc (0.52) and M10_Prsc_SecOrg (0.61), which do not
500 overestimate the concentration in the same way. However, it is clear from the time series that the simulation with iodic acid NPF (IA_BL, IA_BL_SecOrg, IA_BL_M10_ALL) capture the nucleation concentration peaks from NPF events in a way that the M10_Prsc simulations do not. Simulation IA_BL_M10_ALL has the highest overlap index of all simulations for the Aitken mode in the freeze period (0.77), as it is the only simulation to capture the highest values of Aitken concentration during that time.

505 **5   Discussion and conclusion**

We have used field observations and a global aerosol-climate model with an empirical iodic acid nucleation scheme to investigate sources of aerosol in the high Arctic summer. Our results point to a regime transition occurring in late summer from a free-tropospheric source of secondary particles to local boundary layer new particle formation driven by iodic acid. The onset of iodic acid new particle formation (triggered by sea ice freeze-up) coincides with a decline in the free tropospheric source
510 rate brought on by declining rates of photochemical production of precursor vapours in the free troposphere. The net effect of the transition from free troposphere to boundary layer nucleation is a fairly constant nucleation and Aitken mode at the surface.

There are several key conclusions we can draw from the simulations we have presented here. They are listed below.

– The default settings of the UKESM1 model cannot capture Arctic aerosol concentrations. The nucleation mode particle concentration at the surface is at least an order of magnitude too low in CONTROL compared to AO2018, ASCOS
515 and ATom observations, sometimes underestimating observed concentrations by as much as 5 orders of magnitude. The surface Aitken mode concentration is also underestimated by up to 3 orders of magnitude. The model performs better at simulating the surface accumulation mode concentration. The accumulation mode concentration in CONTROL is generally within the range of the observations, but does not capture the lowest concentrations (less than 1 cm^{-3}) seen in the time series of AO2018 observations. These periods of low accumulation mode concentration are important in
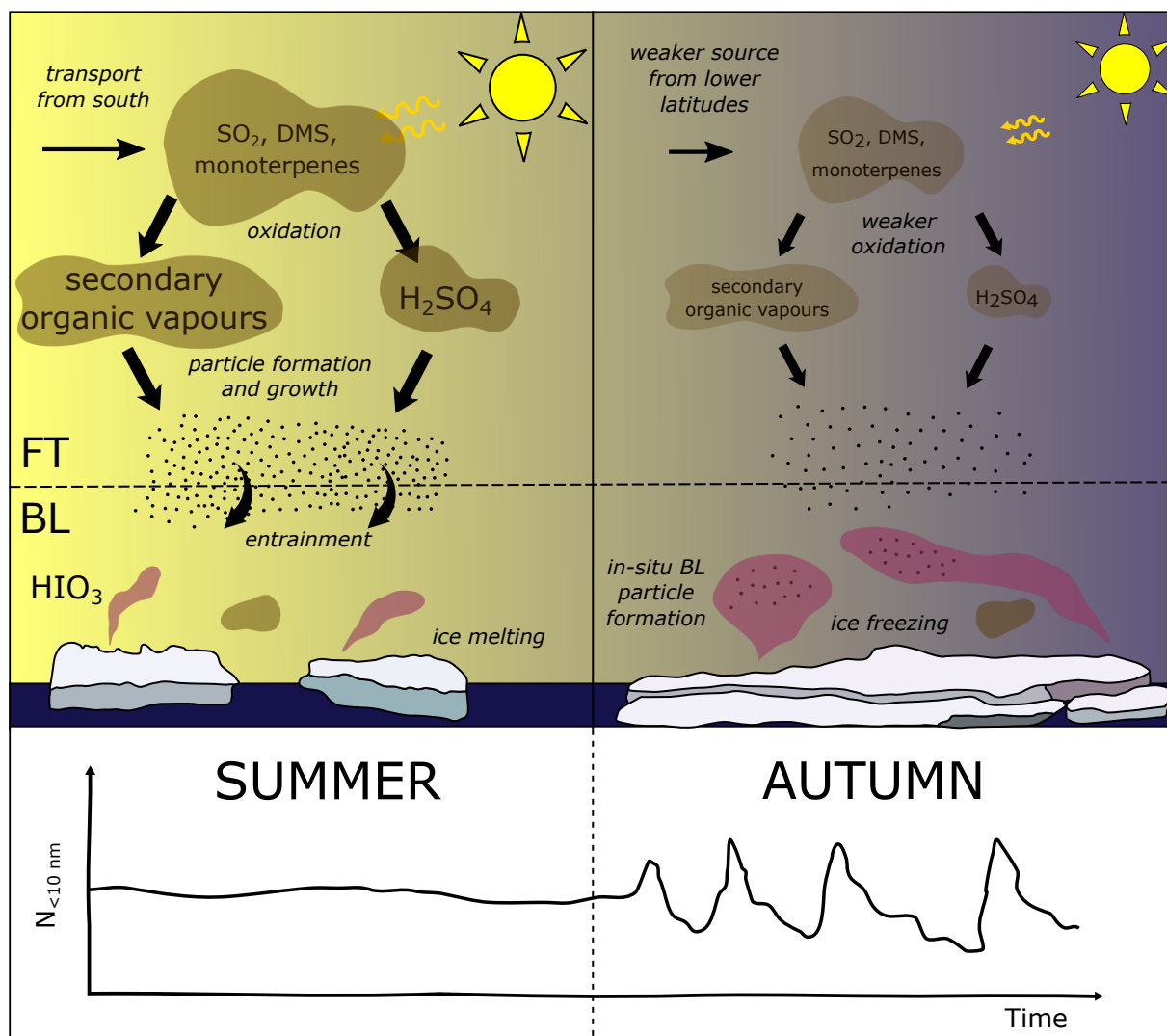
Figure 8. Schematic of processes controlling the concentration of nucleation mode particles at the surface in the high Arctic. The summer sea ice melt period is on the left and the freeze-up period in late summer/early autumn is on the right. A cartoon of the nucleation mode particle concentration is shown at the bottom.

520   controlling the behaviour and radiative effects of low-level Arctic clouds (Mauritsen et al., 2011; Loewe et al., 2017; Birch et al., 2012; Stevens et al., 2018).

– Simulations with H_2SO_4 or organically-mediated boundary layer new particle formation produce more accurate nucleation and Aitken mode concentrations at the surface during the AO2018 melt period than the CONTROL simulation. However, modelled aerosol concentrations aloft as well as output from a simulation where boundary layer new particle formation is switched on only north of 85°N show that little to no boundary layer new particle formation takes place

525

in situ during the AO2018 before the iodic acid new particle formation events occur. This is in contrast to results from Browse et al. (2014), who found that new particle formation from H_2SO_4 in the Arctic boundary layer was an important source of high-Arctic CCN in GLOMAP. Instead, the UKESM simulations with boundary layer new particle formation schemes cause more particles to be created at lower latitudes. These small particles are then transported north through the free troposphere, and provide a source of Aitken mode particles to the surface in the high Arctic. Higher concentrations at the surface from a simulation with a prescribed new particle formation rate in the low free troposphere supports the hypothesis of a free tropospheric source to the surface (Fig. 8, left-hand side).

– Our simulations suggest that a seasonal regime shift triggered by changes in photochemistry coincides with the beginning of the iodic acid season triggered by the sea ice freeze-up. This is portrayed in Fig. 8. The net effect of these two changes is a consistent source of particles controlled by new particle formation. Photochemistry declines towards the end of the AO2018 campaign period as a result of the reduction in incoming solar radiation at the end of summer. In the model output from simulation CONTROL, surface concentrations of the OH radical decline by 87.7% over 80–90°N from August 2018, causing H_2SO_4 to decline by 85.2% while SO_2 increases in concentration in the region by 135.2% over the same period (Table 3). The reduction in H_2SO_4 inhibits new particle formation and particle growth (Fig. D3). In simulation M10_Prsc, the Aitken mode particle concentration declines from August to September 2018 even though the main source of these particles (new particle formation in the free troposphere) is prescribed to be constant. This behaviour highlights the importance of particle growth rates, which can vary alongside the new particle formation rate itself.

Our results have implications for the future Arctic aerosol budget. Iodic acid new particle formation in the Arctic boundary layer is strongly coupled to the surface and therefore sensitive to changes in the sea ice. However, our simulations show that entrainment of secondary particles from the free troposphere is also an important source of surface aerosol at Aitken mode sizes. Free-tropospheric new particle formation is unlikely to have such a strong sensitivity to local sea ice changes, since the precursor vapours and background aerosol in the free troposphere are likely to have been transported from other regions. Further work will be required to understand how the balance of boundary layer versus free-tropospheric nucleation will evolve in the changing Arctic, since predictions of cloud behaviour and surface energy balance in the future Arctic depend on knowledge of the Arctic aerosol budget. It is also important to assess the influence of boundary layer versus free-tropospheric sources compared to other uncertain Arctic aerosol processes and their different representations in models, for example sea spray parameterisations and primary marine sources.

A greater understanding of aerosol conditions in the Arctic free troposphere is needed. It is not possible to distinguish from the model output presented here whether particles coming from the free troposphere have been created there by new particle formation or have first been transported from lower latitudes, where they were created in the boundary layer. Our results indicate the importance of obtaining measurements of aerosol size distributions and precursor vapours from above the boundary layer in the high Arctic, which have previously been sparse. Moreover, the Kulmala et al. (2006) H_2SO_4 and Metzger et al. (2010) organically-mediated new particle formation schemes we use produce very similar surface particle concentrations in the region

560 of study, such that we cannot use these datasets to evaluate the accuracy of one over the other. This highlights an open question in modelling of Arctic aerosol. It is crucial to understand which precursor species are important for Arctic aerosol in order to understand how changes to different parts of the climate system will affect the formation and behaviour of Arctic clouds. The production of secondary organic vapour in UKESM1 is crude, accounting only for the oxidation of monoterpenes, and we have not included any effects of ammonia, which has been shown in laboratory and Arctic field studies to contribute to new

565 particle formation. The inclusion of ammonia in the model could lead to more new particle formation in the boundary layer since ammonia can stabilise H_2SO_4 clusters. However, before these potential sources of model bias can be improved, more observational data is needed about what drives new particle formation throughout the Arctic, both in the free troposphere and at the surface.

The accumulation mode in the model is relatively unaffected by the different new particle formation schemes we used, and

570 is better simulated than the smaller modes. This shows that accumulation mode aerosol and the contribution of the particles to CCN is not affected by new particle formation. However, comparison with AO2018 observations shows that the model cannot capture periods of up to a day of very low accumulation mode concentration (approximately 1 cm^{-3} and below). Given that the accumulation mode affects new particle formation via the sink of condensable vapours, it will be important to consider this model bias in future work. Moreover, observations indicate the importance of fog as a sink of the iodic acid, so more work is

575 needed to assess the role of fog in controlling the frequency of iodic acid new particle formation events. A higher resolution model with better cloud parameterisations would be better suited to such studies than the coarse, global model we have used here.

Code availability. The code used to analyse model output and produce the figures is available on Github at https://github.com/ruthprice/price-acp-figures.

580 *Data availability.* Data from the Arctic Ocean 2018 campaign is available on the Bolin Data Centre, https://bolin.su.se/data/oden-ao-2018-expedition-2. The data used here from the ASCOS campaign is available at www.ascos.se. All data from the Atmospheric Tomography mission are openly available and archived in the Oak Ridge National Laboratory Distributed Active Archive Center (ORNL DAAC) at https://doi.org/10.3334/ORNLDAAC/1925.

Appendix A: Surface temperature during AO2018
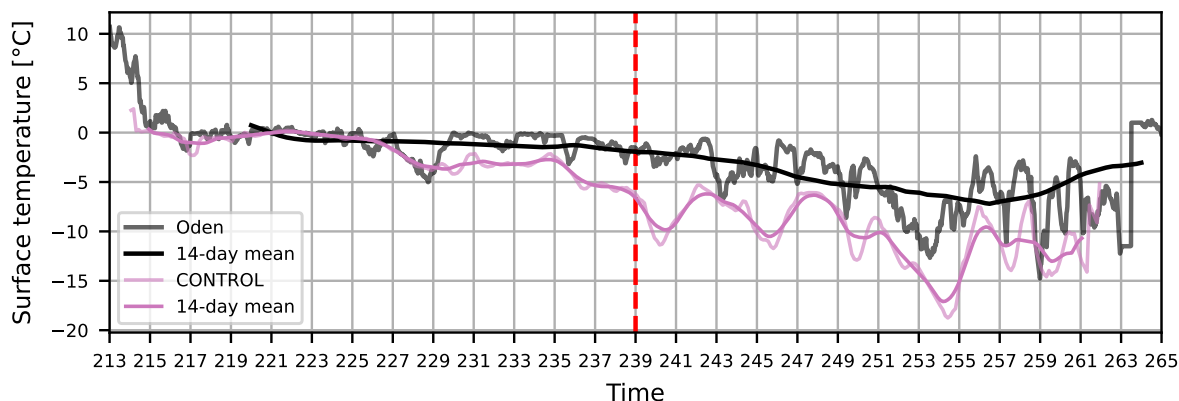
Figure A1. Time series of surface temperature during the AO2018 campaign periods from observations and simulation CONTROL. Observations are shown as 30-min mean values (grey line) and 14-day running mean values (black line). Model output is shown as 3-hourly mean values (pale pink line) and 14-day running mean values (dark pink line). The observed sea ice freeze-up point (when the 14-day mean reaches -2 °C) is marked with a red dashed line.

585   Figure A1 shows the surface temperature during AO2018 from ship measurements and CONTROL output. The sea ice freeze-up point is defined to be when the 14-day running mean of the surface temperature reaches -2 °C. During AO2018, this occurred on 27th August 2018 (day 239). The model output at this time gives a surface temperature of approximately -6 °C. We use -5 °C as the proxy for sea ice freezing in the iodic acid scheme instead of -2 °C, so that the iodic acid is triggered on roughly the observed freeze-up day in the model.

590 **Appendix B: Particle ageing**

In Sect. 4.2 we show that K06_BL and M10_BL simulate more accurate concentrations of the nucleation and Aitken modes during AO2018 than simulation CONTROL (3). Figure B1 shows the surface aerosol concentrations for simulations UKESM_default and CONTROL, K06_BL_default and K06_BL, and M10_BL_default and M10_BL. The simulations with the ageing change produce higher concentrations in the nucleation and Aitken modes than the DEFAULT simulations, and this difference is
595 greater in the simulations with BL NPF than it is between UKESM_DEFAULT and CONTROL. This is because the mode merging described in Sect. 3.4 affects the Aitken mode concentration more when there is a stronger source of smaller particles. In the Aitken mode, the concentrations from simulations K06_BL and M10_BL are typically higher than K06_BL_DEFAULT and M10_BL_DEFAULT by a factor of 2–10. The model-observation agreement is therefore improved in simulations with the ageing change.
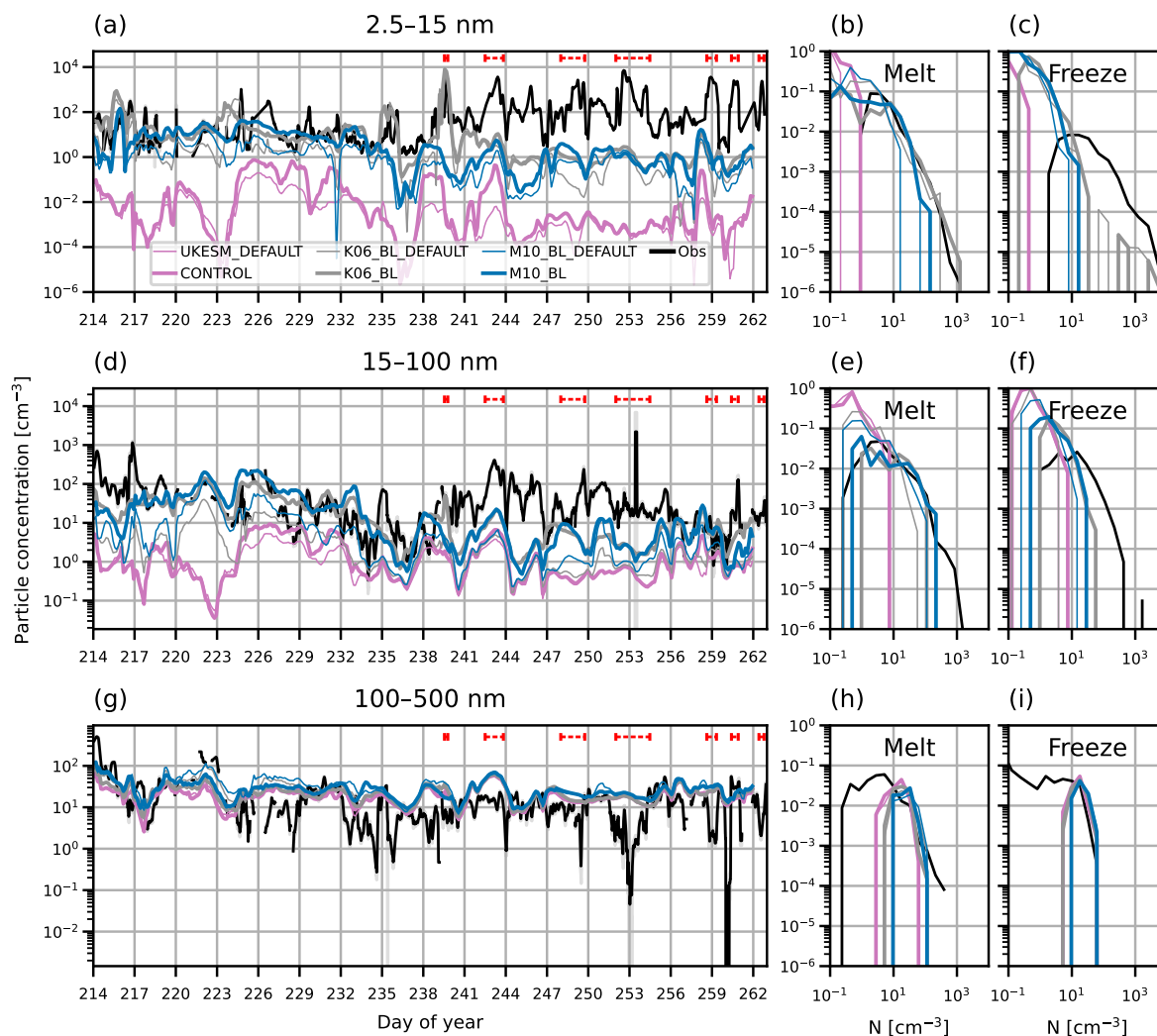
Figure B1. Time series and PDFs of surface aerosol concentration during AO2018 from observations and model output. Model output is from simulations UKESM_DEFAULT (thin pink lines), CONTROL (thick pink lines), K06_BL_DEFAULT (think grey lines), K06_BL (thick grey lines), M10_BL_DEFAULT (thin blue lines) and M10_BL (thick blue lines). Observations are shown as 3-hourly mean (black lines) and standard deviation (grey shading). Aerosol concentrations are shown for particles with diameter (a–c) 2.5–15 nm, (d–f) 15–100 nm and (g–i) 100–500 nm. Red dashed lines in (a, d, g) show observed NPF events. PDFs are separated by observed sea ice freeze-up date, 27th August 2018 (day 239).

600   Figure B2 shows mean aerosol profiles simulated for the AO2018 period for the soluble nucleation, Aitken and accumulation modes and the insoluble mode. Model output is shown for simulations CONTROL, UKESM_default, K06_BL(_default) M10_BL(_default), M10_FT(_default), M10_ALL(_default) and M10_Prsc(_default). The perturbed ageing scheme produces
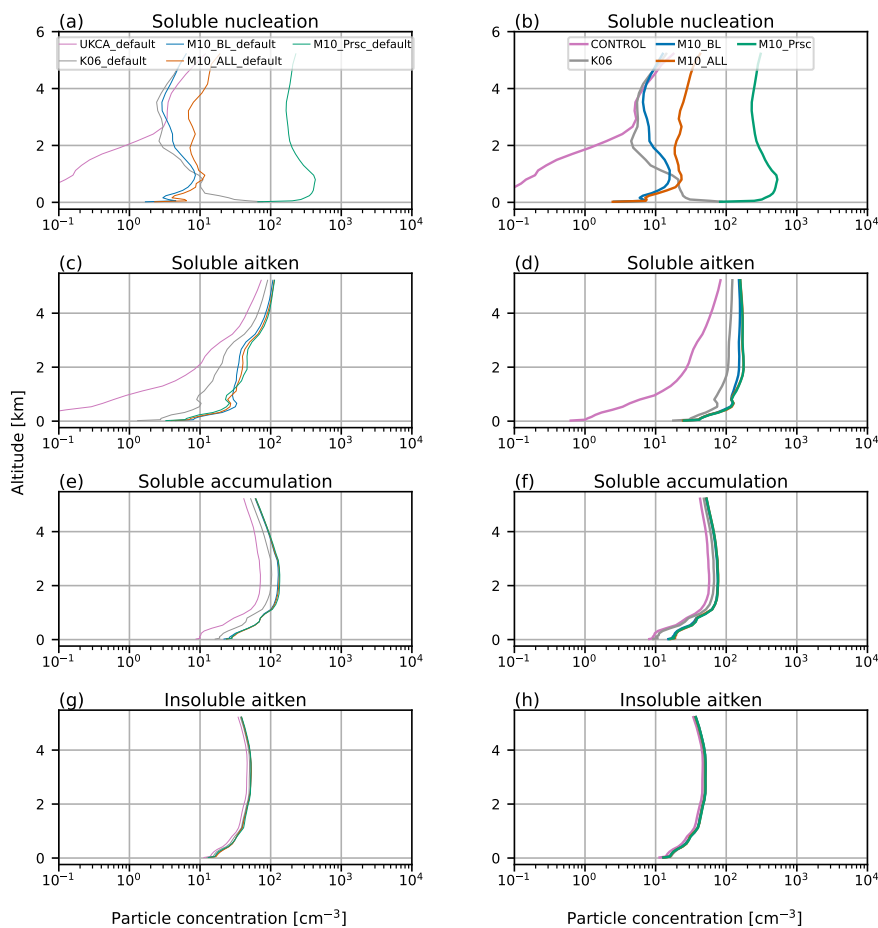
Figure B2. Mean simulated aerosol profiles for AO2018 campaign period. Concentrations shown are for (a–b) soluble nucleation, (c–d) soluble Aitken, (e–f) soluble accumulation and (g–h) insoluble Aitken modes. Model output is from simulations UKCA_DEFAULT and CONTROL (pink lines), K06_BL_default and K06_BL (grey lines), M10_ALL_default and M10_ALL (red lines), M10_BL_default and M10_BL (dark blue lines) and M10_Prsc_default and M10_Prsc (green lines).

up to an order of magnitude more Aitken mode particles than the default scheme in the low FT and at the surface, independently of which NPF scheme is used. The insoluble mode is not significantly affected by the changes to the ageing scheme.
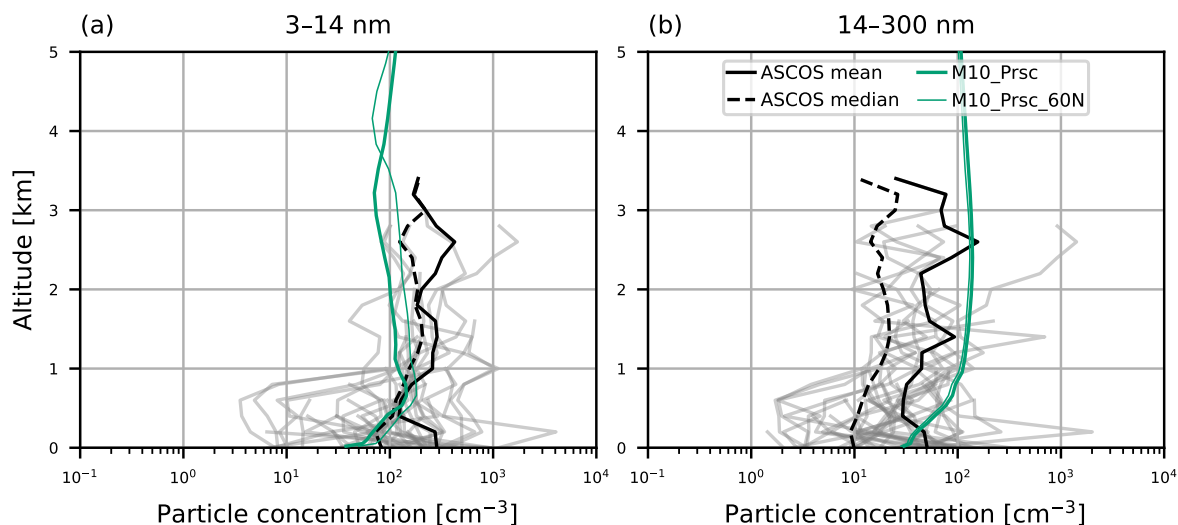
Figure C1. Aerosol vertical profiles from model output and ASCOS campaign observations. Model output is from colocated monthly mean values from simulations M10_Prsc (thick dark green) and M10_Prsc_60N (thin dark green). Observed values are given as the mean profile from each ASCOS flight (grey lines), overall mean (solid black) and overall median (dashed black). Profiles are for particles with size (a) 3–14 nm, measured during ASCOS using a UCPC and (b) 14–300 nm, measured using a CPC (particles greater than 14 nm) and a CLASP instrument (particles greater than 300 nm).

Appendix C: Latitude limit for prescribed FT NPF rate

In simulation M10_Prsc, we impose a NPF rate of 10^{-2} cm^{-3} s^{-1} in model levels between the top of the boundary layer and 7.5 km altitude. The rate is imposed in gridboxes north of 80°N. In Sect. 4.3.1 we compare the M10_Prsc output to aerosol profiles from the ASCOS and ATom campaigns to test how realistic such a NPF rate may be. However, the data we use from ATom was taken further south, between approximately 60–80°N (see Fig. 1). To test our prescribed FT NPF rate using ATom observations we therefore ran another simulation, M10_Prsc_60N, where the rate is imposed north of 60 °N.

Figures C1 and C2 show output from M10_Prsc and M10_Prsc_60N with observations from ASCOS and ATom. Aerosol concentrations from the two simulations are within an order of magnitude of each other. While the prescribed rate increases aerosol concentrations relative to CONTROL in the ASCOS region (Sect. 4.3.1), it makes little difference in the ATom region even when we extend the region in which the rate is applied. This is likely because NPF rates are already higher in the ATom region than the ASCOS region due to the relative proximity of ATom to open water and boreal forests, both of which supply precursor vapours to the atmosphere.
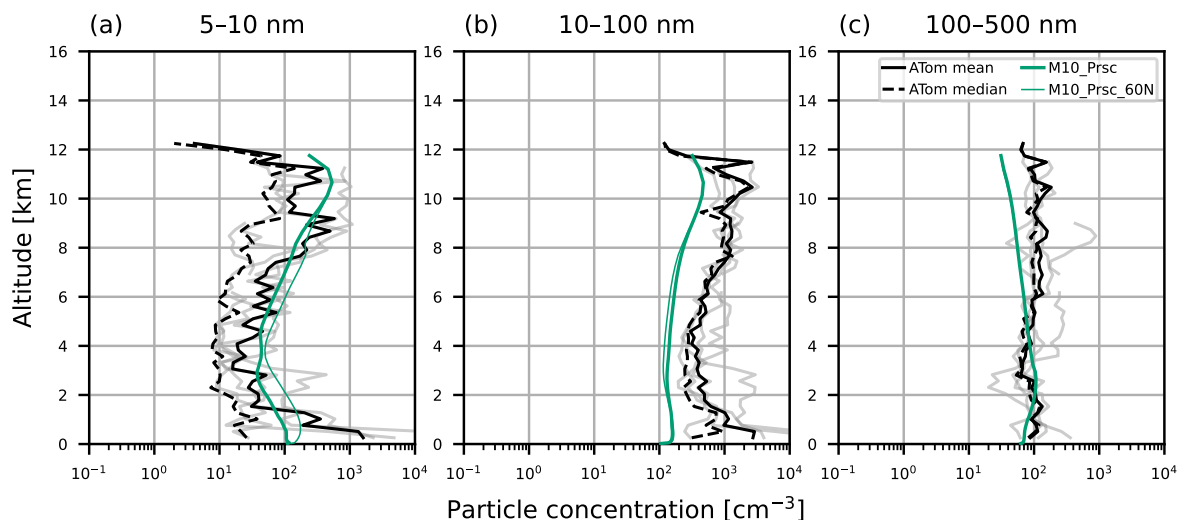
Figure C2. Aerosol vertical profiles from model output and ATom campaign observations. Model output is from colocated monthly mean values from simulations M10_Prsc (thick dark green) and M10_Prsc_60N (thin dark green). ATom observations are taken from leg 1 of the campaign and restricted to measurements that were taken north of 60°N. Observations correspond to mean profiles from different days (grey lines), the overall mean (black solid lines) and overall median (black dashed lines). Profiles are for particles with size (a) 5–10 nm, (b) 10–100 nm and (c) 100–500 nm. Observations were recorded at standard temperature and pressure, model output has been adjusted to account for this.

Appendix D: Aerosol precursor vapours and growth rate

Figures D1 and D2 show maps and zonal means of H_2SO_4 and secondary organic vapour concentration from simulation CONTROL. In August, Arctic H_2SO_4 concentration peaks just above the surface and at approximately 8 km (Fig. D1(a)). The concentration decreases throughout most of the troposphere from August to September by at least an order of magnitude. In August, the secondary organics have a maximum at the surface from 60–70°N and some of this plume spreads north to the high Arctic. Unlike H_2SO_4, concentrations do not significantly reduce from August to September. The mean surface concentration of H_2SO_4 for 80–90°N reduces by 85.2% from August to September, while for secondary organics the reduction is only 5.9%. Percentage changes for other vapours are given in Table 3.

The decline in vapour concentration from August to September drives a reduction in the growth rate of aerosols from condensation of vapour. Figure D3 shows aerosol growth rates calculated from model output from simulation CONTROL. Arctic growth rates are lower than in the mid-latitudes and tropics, where H_2SO_4 and secondary organics have higher concentrations. In the central Arctic, the decreasing growth rate is driven by the decrease in H_2SO_4. Secondary organic vapours contribute little to the growth rate in the central Arctic region, but dominate in the continental Arctic in North America and northern Eurasia, where concentrations are high near the boreal forest source regions.

In Sect. 4.3.2 we showed that the source of aerosols from FT NPF weakens towards the end of summer. This occurs even when the FT NPF rate is held constant in time as in simulation M10_Prsc. The slower aerosol growth rate shown in Fig. D3 curbs FT NPF in September. This highlights that it is important to understand the growth of new particles as well as their formation.
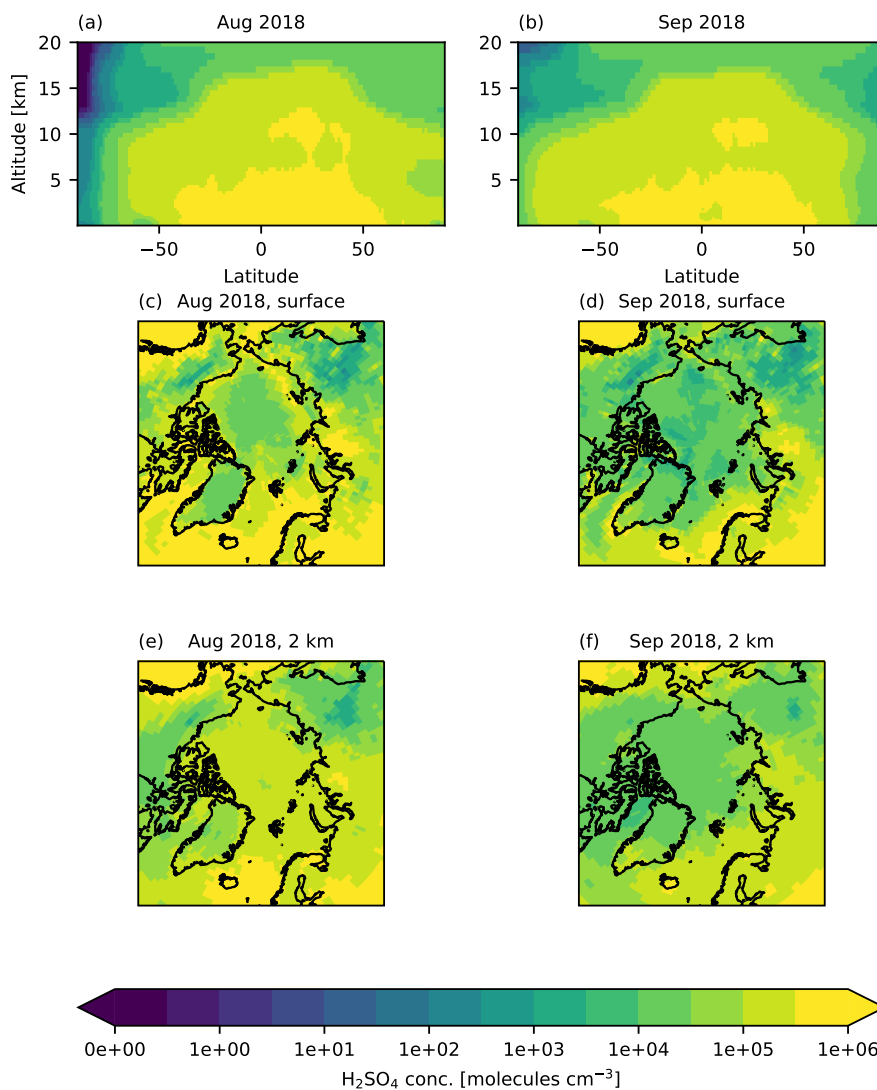
Figure D1. Zonal means and maps of simulated monthly mean H_2SO_4 concentration from simulation CONTROL. Maps are taken from model level (c–d) at surface and (e–f) with altitude 2 km.
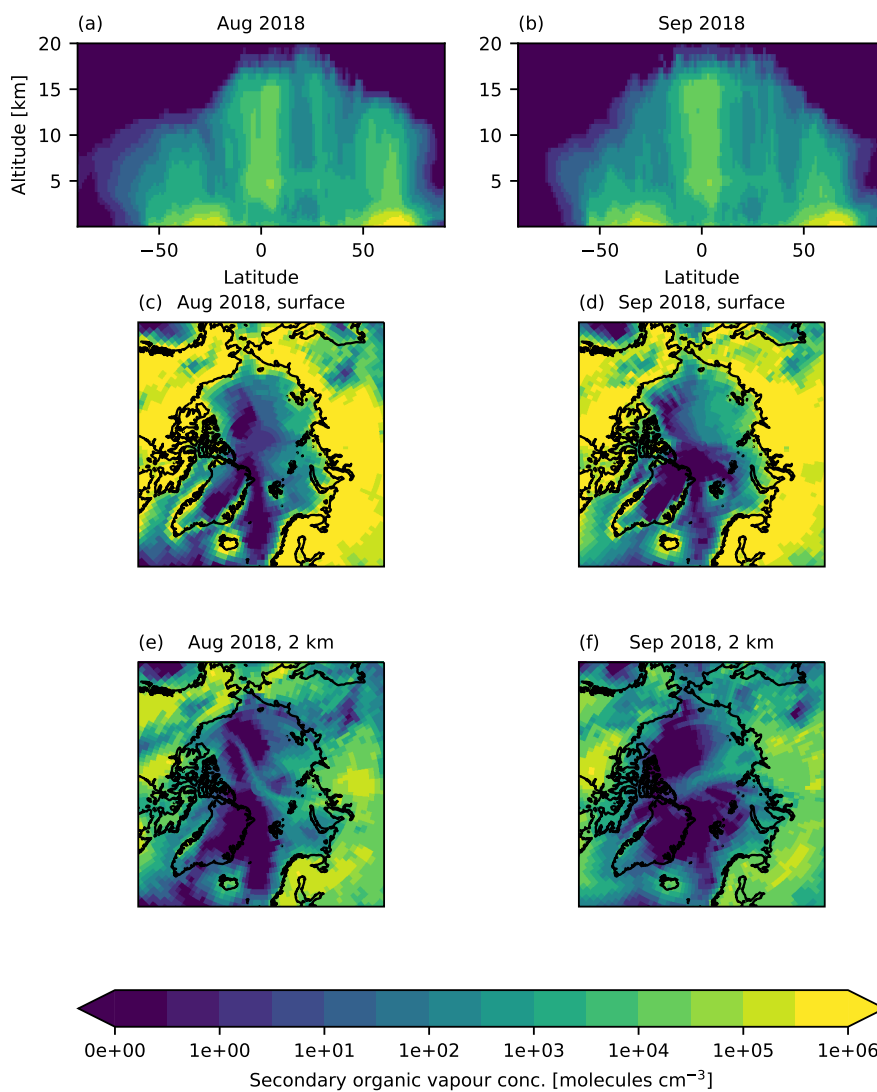
Figure D2. Zonal means and maps of simulated monthly mean secondary organic vapour concentration from simulation CONTROL. Maps are taken from model level (c–d) sat surface and (e–f) with altitude 2 km.
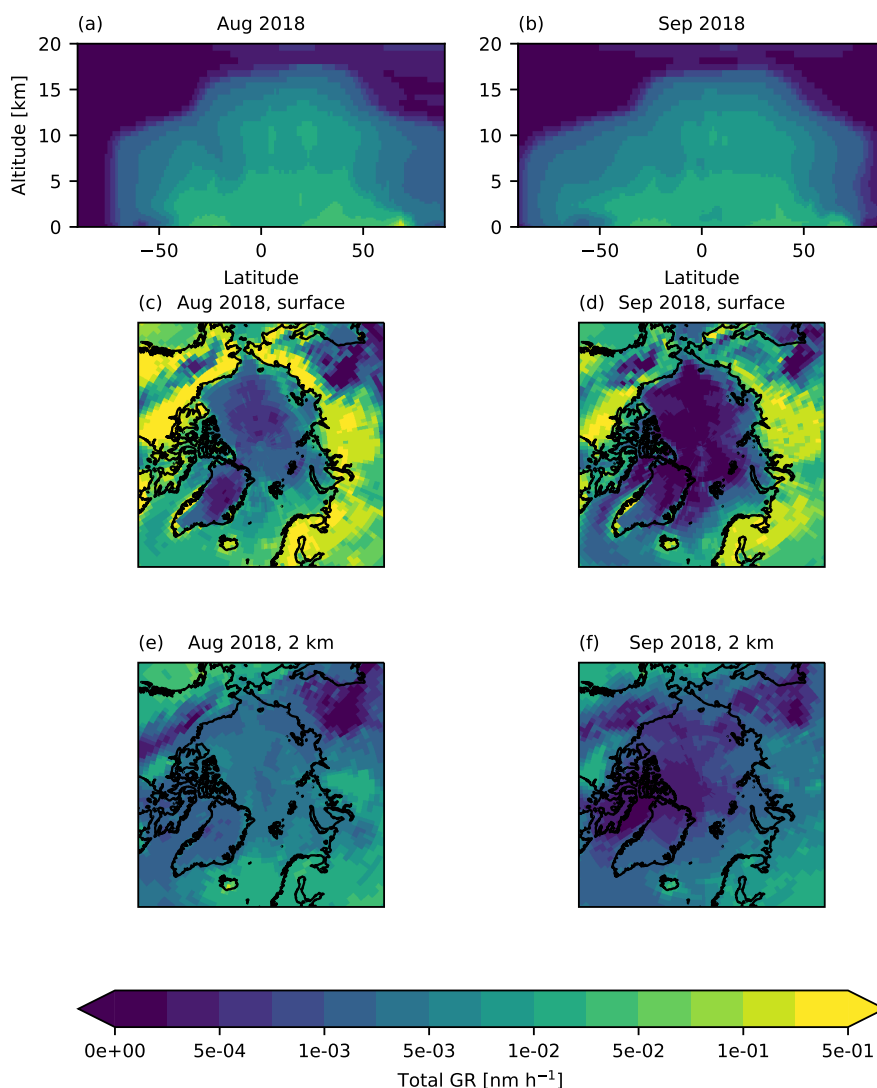
Figure D3. Zonal means and maps of aerosol growth rates from simulation CONTROL. Growth rates are calculated offline using model output of temperature and concentrations of H_2SO_4 and secondary organic vapour. Maps are taken from model level (c–d) at surface and (e–f) with altitude 2 km.

635 *Author contributions.* RP ran model simulations, assisted by PF, and analysed output with guidance from KSC. JS, AB and PZ performed aerosol measurements during AO2018. RP, PF, IMB and KSC contributed towards the design of the study. All authors were involved in discussion of results and writing of the manuscript.

Competing interests. KSC is an executive editor of ACP. The peer-review process was guided by an independent editor, and the authors have also no other competing interests to declare.

640   *Acknowledgements.* RP was supported by a Natural Environment Research Council (NERC) Ph.D. studentship through the SPHERES Doctoral Training Partnership (NE/L002574/1). PZ was supported by the Swedish Research Council (VR starting grant 2018-05045). JS and AB received funding from the Swiss National Science Foundation (Grant no. 169090) and the Swiss Polar Institute. JS holds the Ingvar Kamprad Chair for Extreme Environments Research sponsored by Ferring Pharmaceuticals. KSC was funded by the NERC project A-CURE (NE/P013406/1). IMB was funded by NERC (grant No. NE/R009686/1)

645   We thank Hamish Gordon for his advice on new particle formation schemes in the model. We acknowledge use of the Monsoon2 system, a collaborative facility supplied under the Joint Weather and Climate Research Programme, a strategic partnership between the Met Office and the Natural Environment Research Council. This work used JASMIN, the UK's collaborative data analysis environment (https://jasmin.ac.uk).

References

650   Allan, J. D., Williams, P. I., Najera, J., Whitehead, J. D., Flynn, M. J., Taylor, J. W., Liu, D., Darbyshire, E., Carpenter, L. J., Chance, R., Andrews, S. J., Hackenberg, S. C., and McFiggans, G.: Iodine observed in new particle formation events in the Arctic atmosphere during ACCACIA, Atmospheric Chemistry and Physics, 15, 5599–5609, https://doi.org/10.5194/acp-15-5599-2015, 2015.

Alterskjær, K., Kristjánsson, J. E., and Hoose, C.: Do anthropogenic aerosols enhance or suppress the surface cloud forcing in the Arctic?, Journal of Geophysical Research Atmospheres, 115, https://doi.org/10.1029/2010JD014015, 2010.

655   AMAP: Arctic Climate Change Update 2021: Key Trends and Impacts. Summary for Policy-makers, Arctic Monitoring and Assessment Programme (AMAP), Trømso, Norway, 2021.

Baccarini, A. and Schmale, J.: Ultrafine particle concentration measured during the Arctic Ocean 2018 expedition [data set], https://doi.org/10.17043/oden-ao-2018-aerosol-ufp-1, 2020.

Baccarini, A., Karlsson, L., Dommen, J., Duplessis, P., Vüllers, J., Brooks, I. M., Saiz-Lopez, A., Salter, M., Tjernström, M., Baltensperger,
660   U., Zieger, P., and Schmale, J.: Frequent new particle formation over the high Arctic pack ice by enhanced iodine emissions, Nature Communications, 11, 4924, https://doi.org/10.1038/s41467-020-18551-0, 2020a.

Baccarini, A., Schmale, J., and Dommen, J.: Iodic acid, sulfuric acid and methanesulfonic acid collected during the Arctic Ocean 2018 expedition [data set], https://doi.org/10.17043/oden-ao-2018-aerosol-cims-1, 2020b.

Beck, L. J., Sarnela, N., Junninen, H., Hoppe, C. J. M., Garmash, O., Bianchi, F., Riva, M., Rose, C., Per akyl a, O., Wimmer, D., Kausiala,
665   O., Jokinen, T., Ahonen, L., Mikkil a, J., Hakala, J., He, X., Kontkanen, J., Wolf, K. K. E., Cappelletti, D., Mazzola, M., Traversi, R., Petroselli, C., Viola, A. P., Vitale, V., Lange, R., Massling, A., Nojgaard, J. K., Krejci, R., Karlsson, L., Zieger, P., Jang, S., Lee, K., Vakkari, V., Lampilahti, J., Thakur, R. C., Leino, K., Kangasluoma, J., Duplissy, E., Siivola, E., Marbouti, M., Tham, Y. J., Saiz-Lopez, A., Pet aj a, T., Ehn, M., Worsnop, D. R., Skov, H., Kulmala, M., Kerminen, V., and Sipil a, M.: Differing mechanisms of new particle formation at two Arctic sites., Geophysical Research Letters, https://doi.org/10.1029/2020gl091334, 2020.

670   Bigg, E. K. and Leck, C.: Cloud-active particles over the central Arctic Ocean, Journal of Geophysical Research: Atmospheres, 106, 32 155– 32 166, https://doi.org/10.1029/1999JD901152, 2001.

Bigg, K. E., Leck, C., and Nilsson, D. E.: Sudden changes in arctic atmospheric aerosol concentrations during summer and autumn, Tellus B: Chemical and Physical Meteorology, 48, 254–271, https://doi.org/10.3402/tellusb.v48i2.15890, 1996.

Birch, C. E., Brooks, I. M., Tjernström, M., Shupe, M. D., Mauritsen, T., Sedlar, J., Lock, A. P., Earnshaw, P., Persson, P. O. G., Milton, S. F.,
675   and Leck, C.: Modelling atmospheric structure, cloud and their response to CCN in the central Arctic: ASCOS case studies, Atmospheric Chemistry and Physics, 12, 3419–3435, https://doi.org/10.5194/acp-12-3419-2012, 2012.

Biskaborn, B. K., Smith, S. L., Noetzli, J., Matthes, H., Vieira, G., Streletskiy, D. A., Schoeneich, P., Romanovsky, V. E., Lewkowicz, A. G., Abramov, A., Allard, M., Boike, J., Cable, W. L., Christiansen, H. H., Delaloye, R., Diekmann, B., Drozdov, D., Etzelm uller, B., Grosse, G., Guglielmin, M., Ingeman-Nielsen, T., Isaksen, K., Ishikawa, M., Johansson, M., Johannsson, H., Joo, A., Kaverin, D., Kholodov, A.,
680   Konstantinov, P., Kr oger, T., Lambiel, C., Lanckman, J. P., Luo, D., Malkova, G., Meiklejohn, I., Moskalenko, N., Oliva, M., Phillips, M., Ramos, M., Sannel, A. B. K., Sergeev, D., Seybold, C., Skryabin, P., Vasiliev, A., Wu, Q., Yoshikawa, K., Zheleznyak, M., and Lantuit, H.: Permafrost is warming at a global scale, Nature Communications, 10, https://doi.org/10.1038/s41467-018-08240-4, 2019.

Brock, C. A., Williamson, C., Kupc, A., Froyd, K. D., Erdesz, F., Wagner, N., Richardson, M., Schwarz, J. P., Gao, R. S., Katich, J. M., Campuzano-Jost, P., Nault, B. A., Schroder, J. C., Jimenez, J. L., Weinzierl, B., Dollner, M., Bui, T., and Murphy, D. M.: Aerosol size

685   distributions during the Atmospheric Tomography Mission (ATom): Methods, uncertainties, and data products, Atmospheric Measurement
       Techniques, 12, 3081–3099, https://doi.org/10.5194/amt-12-3081-2019, 2019.

       Browse, J., Carslaw, K. S., Arnold, S. R., Pringle, K., and Boucher, O.: The scavenging processes controlling the seasonal cycle in Arctic
       sulphate and black carbon aerosol, Atmospheric Chemistry and Physics, 12, 6775–6798, https://doi.org/10.5194/acp-12-6775-2012, 2012.

       Browse, J., Carslaw, K. S., Mann, G. W., Birch, C. E., Arnold, S. R., and Leck, C.: The complex response of Arctic aerosol to sea-ice retreat,
690   Atmospheric Chemistry and Physics, 14, 7543–7557, https://doi.org/10.5194/acp-14-7543-2014, 2014.

       Bulatovic, I., Igel, A. L., Leck, C., Heintzenberg, J., Riipinen, I., and Ekman, A. M. L.: The importance of Aitken mode aerosol particles
       for cloud sustenance in the summertime high Arctic – a simulation study supported by observational data, Atmospheric Chemistry and
       Physics, 21, 3871–3897, https://doi.org/10.5194/acp-21-3871-2021, 2021.

       Cazenave, A., Meyssignac, B., Ablain, M., Balmaseda, M., Bamber, J., Barletta, V., Beckley, B., Benveniste, J., Berthier, E., Blazquez, A.,
695   Boyer, T., Caceres, D., Chambers, D., Champollion, N., Chao, B., Chen, J., Cheng, L., Church, J. A., Chuter, S., Cogley, J. G., Dangendorf,
       S., Desbruyères, D., D oll, P., Domingues, C., Falk, U., Famiglietti, J., Fenoglio-Marc, L., Forsberg, R., Galassi, G., Gardner, A., Groh,
       A., Hamlington, B., Hogg, A., Horwath, M., Humphrey, V., Husson, L., Ishii, M., Jaeggi, A., Jevrejeva, S., Johnson, G., Kolodziejczyk,
       N., Kusche, J., Lambeck, K., Landerer, F., Leclercq, P., Legresy, B., Leuliette, E., Llovel, W., Longuevergne, L., Loomis, B. D., Luthcke,
       S. B., Marcos, M., Marzeion, B., Merchant, C., Merrifield, M., Milne, G., Mitchum, G., Mohajerani, Y., Monier, M., Monselesan, D.,
700   Nerem, S., Palanisamy, H., Paul, F., Perez, B., Piecuch, C. G., Ponte, R. M., Purkey, S. G., Reager, J. T., Rietbroek, R., Rignot, E., Riva,
       R., Roemmich, D. H., Sørensen, L. S., Sasgen, I., Schrama, E. J., Seneviratne, S. I., Shum, C. K., Spada, G., Stammer, D., van de Wal, R.,
       Velicogna, I., von Schuckmann, K., Wada, Y., Wang, Y., Watson, C., Wiese, D., Wijffels, S., Westaway, R., Woppelmann, G., and Wouters,
       B.: Global sea-level budget 1993-present, Earth System Science Data, 10, 1551–1590, https://doi.org/10.5194/essd-10-1551-2018, 2018.

       Chang, R. Y., Sjostedt, S. J., Pierce, J. R., Papakyriakou, T. N., Scarratt, M. G., Michaud, S., Levasseur, M., Leaitch, W. R., and Abbatt,
705   J. P.: Relating atmospheric and oceanic DMS levels to particle nucleation events in the Canadian Arctic, Journal of Geophysical Research
       Atmospheres, 116, https://doi.org/10.1029/2011JD015926, 2011.

       Croft, B., Wentworth, G. R., Martin, R. V., Leaitch, W. R., Murphy, J. G., Murphy, B. N., Kodros, J. K., Abbatt, J. P., and Pierce, J. R.:
       Contribution of Arctic seabird-colony ammonia to atmospheric particles and cloud-albedo radiative effect, Nature Communications, 7,
       https://doi.org/10.1038/ncomms13444, 2016.

710   Croft, B., Martin, R. V., Leaitch, W. R., Burkart, J., Chang, R. Y.-W., Collins, D. B., Hayes, P. L., Hodshire, A. L., Huang, L., Kodros, J. K.,
       Moravek, A., Mungall, E. L., Murphy, J. G., Sharma, S., Tremblay, S., Wentworth, G. R., Willis, M. D., Abbatt, J. P. D., and Pierce,
       J. R.: Arctic marine secondary organic aerosol contributes significantly to summertime particle size distributions in the Canadian Arctic
       Archipelago, Atmospheric Chemistry and Physics, 19, 2787–2812, https://doi.org/10.5194/acp-19-2787-2019, 2019.

       Curry, J. A., Schramm, J. L., and Ebert, E. E.: Impact of clouds on the surface radiation balance of the Arctic Ocean, Meteorology and
715   Atmospheric Physics, 51, 197–217, https://doi.org/10.1007/BF01030494, 1993.

       Dall'Osto, M., Beddows, D. C., Tunved, P., Krejci, R., Str om, J., Hansson, H. C., Yoon, Y. J., Park, K. T., Becagli, S., Udisti, R., Onasch,
       T., O'dowd, C. D., Simó, R., and Harrison, R. M.: Arctic sea ice melt leads to atmospheric new particle formation, Scientific Reports, 7,
       https://doi.org/10.1038/s41598-017-03328-1, 2017.

       Dall'Osto, M., Geels, C., Beddows, D. C., Boertmann, D., Lange, R., Nojgaard, J. K., Harrison, R. M., Simo, R., Skov, H., and
720   Massling, A.: Regions of open water and melting sea ice drive new particle formation in North East Greenland, Scientific Reports, 8,
       https://doi.org/10.1038/s41598-018-24426-8, 2018.

Engvall, A.-C., Krejci, R., Ström, J., Minikin, A., Treffeisen, R., Stohl, A., and Herber, A.: In-situ airborne observations of the microphysical properties of the Arctic tropospheric aerosol during late spring and summer, Tellus B: Chemical and Physical Meteorology, 60, 392–404, https://doi.org/10.1111/j.1600-0889.2008.00348.x, 2008.

Flanner, M. G., Shell, K. M., Barlage, M., Perovich, D. K., and Tschudi, M. A.: Radiative forcing and albedo feedback from the Northern Hemisphere cryosphere between 1979 and 2008, Nature Geoscience, 4, 151–155, https://doi.org/10.1038/ngeo1062, 2011.

Gantt, B., Johnson, M. S., Crippa, M., Prévôt, A. S., and Meskhidze, N.: Implementing marine organic aerosols into the GEOS-Chem model, Geoscientific Model Development, 8, 619–629, https://doi.org/10.5194/gmd-8-619-2015, 2015.

Garrett, T. J. and Zhao, C.: Increased Arctic cloud longwave emissivity associated with pollution from mid-latitudes, Nature, 440, 787–789, https://doi.org/10.1038/nature04636, 2006.

Gilgen, A., Huang, W. T. K., Ickes, L., Neubauer, D., and Lohmann, U.: How important are future marine and shipping aerosol emissions in a warming Arctic summer and autumn?, Atmospheric Chemistry and Physics, 18, 10 521–10 555, https://doi.org/10.5194/acp-18-10521-2018, 2018.

Gong, S. L.: A parameterization of sea-salt aerosol source function for sub- and super-micron particles, Global Biogeochemical Cycles, 17, https://doi.org/10.1029/2003gb002079, 2003.

Gordon, H., Kirkby, J., Baltensperger, U., Bianchi, F., Breitenlechner, M., Curtius, J., Dias, A., Dommen, J., Donahue, N. M., Dunne, E. M., Duplissy, J., Ehrhart, S., Flagan, R. C., Frege, C., Fuchs, C., Hansel, A., Hoyle, C. R., Kulmala, M., K urten, A., Lehtipalo, K., Makhmutov, V., Molteni, U., Rissanen, M. P., Stozhkov, Y., Tr ostl, J., Tsagkogeorgas, G., Wagner, R., Williamson, C., Wimmer, D., Winkler, P. M., Yan, C., and Carslaw, K. S.: Causes and importance of new particle formation in the present-day and preindustrial atmospheres, Journal of Geophysical Research: Atmospheres, 122, 8739–8760, https://doi.org/10.1002/2017JD026844, 2017.

He, X.-C., Tham, Y. J., Dada, L., Wang, M., Finkenzeller, H., Stolzenburg, D., Iyer, S., Simon, M., Kürten, A., Shen, J., Rörup, B., Rissanen, M., Schobesberger, S., Baalbaki, R., Wang, D. S., Koenig, T. K., Jokinen, T., Sarnela, N., Beck, L. J., Almeida, J., Amanatidis, S., Amorim, A., Ataei, F., Baccarini, A., Bertozzi, B., Bianchi, F., Brilke, S., Caudillo, L., Chen, D., Chiu, R., Chu, B., Dias, A., Ding, A., Dommen, J., Duplissy, J., Haddad, I. E., Carracedo, L. G., Granzin, M., Hansel, A., Heinritzi, M., Hofbauer, V., Junninen, H., Kangasluoma, J., Kemppainen, D., Kim, C., Kong, W., Krechmer, J. E., Kvashin, A., Laitinen, T., Lamkaddam, H., Lee, C. P., Lehtipalo, K., Leiminger, M., Li, Z., Makhmutov, V., Manninen, H. E., Marie, G., Marten, R., Mathot, S., Mauldin, R. L., Mentler, B., Möhler, O., Müller, T., Nie, W., Onnela, A., Petäjä, T., Pfeifer, J., Philippov, M., Ranjithkumar, A., Saiz-Lopez, A., Salma, I., Scholz, W., Schuchmann, S., Schulze, B., Steiner, G., Stozhkov, Y., Tauber, C., Tomé, A., Thakur, R. C., Väisänen, O., Vazquez-Pufleau, M., Wagner, A. C., Wang, Y., Weber, S. K., Winkler, P. M., Wu, Y., Xiao, M., Yan, C., Ye, Q., Ylisirniö, A., Zauner-Wieczorek, M., Zha, Q., Zhou, P., Flagan, R. C., Curtius, J., Baltensperger, U., Kulmala, M., Kerminen, V.-M., Kurtén, T., Donahue, N. M., Volkamer, R., Kirkby, J., Worsnop, D. R., and Sipilä, M.: Role of iodine oxoacids in atmospheric aerosol nucleation, http://science.sciencemag.org/, 2021.

Hoesly, R. M., Smith, S. J., Feng, L., Klimont, Z., Janssens-Maenhout, G., Pitkanen, T., Seibert, J. J., Vu, L., Andres, R. J., Bolt, R. M., Bond, T. C., Dawidowski, L., Kholod, N., Kurokawa, J. I., Li, M., Liu, L., Lu, Z., Moura, M. C., O'Rourke, P. R., and Zhang, Q.: Historical (1750-2014) anthropogenic emissions of reactive gases and aerosols from the Community Emissions Data System (CEDS), Geoscientific Model Development, 11, 369–408, https://doi.org/10.5194/gmd-11-369-2018, 2018.

Hugelius, G., Strauss, J., Zubrzycki, S., Harden, J. W., Schuur, E. A., Ping, C. L., Schirrmeister, L., Grosse, G., Michaelson, G. J., Koven, C. D., O'Donnell, J. A., Elberling, B., Mishra, U., Camill, P., Yu, Z., Palmtag, J., and Kuhry, P.: Estimated stocks of circumpolar permafrost carbon with quantified uncertainty ranges and identified data gaps, Biogeosciences, 11, 6573–6593, https://doi.org/10.5194/bg-11-6573-2014, 2014.

760 Karl, M., Leck, C., Gross, A., and Pirjola, L.: A study of new particle formation in the marine boundary layer over the central
     Arctic Ocean using a flexible multicomponent aerosol dynamic model, Tellus, Series B: Chemical and Physical Meteorology, 64,
     https://doi.org/10.3402/tellusb.v64i0.17158, 2012.

Karl, M., Leck, C., Coz, E., and Heintzenberg, J.: Marine nanogels as a source of atmospheric nanoparticles in the high Arctic, Geophysical
     Research Letters, 40, 3738–3743, https://doi.org/https://doi.org/10.1002/grl.50661, 2013.

765 Karlsson, L. and Zieger, P.: Aerosol particle number size distribution data collected during the Arctic Ocean 2018 expedition [data set],
     https://doi.org/10.17043/oden-ao-2018-aerosol-dmps-1, 2020.

Karlsson, L., Krejci, R., Koike, M., Ebell, K., and Zieger, P.: A long-term study of cloud residuals from low-level Arctic clouds, Atmospheric
     Chemistry and Physics, 21, 8933–8959, https://doi.org/10.5194/acp-21-8933-2021, 2021.

Karlsson, L., Baccarini, A., Duplessis, P., Baumgardner, D., Brooks, I. M., Chang, R. Y., Dada, L., D allenbach, K. R., Heikkinen, L., Krejci,
770 R., Leaitch, W. R., Leck, C., Partridge, D. G., Salter, M. E., Wernli, H., Wheeler, M. J., Schmale, J., and Zieger, P.: Physical and Chemical
     Properties of Cloud Droplet Residuals and Aerosol Particles During the Arctic Ocean 2018 Expedition, Journal of Geophysical Research:
     Atmospheres, 127, https://doi.org/10.1029/2021jd036383, 2022.

Kay, J. E., L'Ecuyer, T., Chepfer, H., Loeb, N., Morrison, A., and Cesana, G.: Recent Advances in Arctic Cloud and Climate Research,
     https://doi.org/10.1007/s40641-016-0051-9, 2016.

775 Kerminen, V.-M. and Kulmala, M.: Analytical formulae connecting the "real" and the "apparent" nucleation rate and the nuclei number
     concentration for atmospheric nucleation events, Aerosol Science, 33, 609–622, www.elsevier.com/locate/jaerosci, 2002.

Koike, M., Ukita, J., Str om, J., Tunved, P., Shiobara, M., Vitale, V., Lupi, A., Baumgardner, D., Ritter, C., Hermansen, O., Yamada, K., and
     Pedersen, C. A.: Year-Round In Situ Measurements of Arctic Low-Level Clouds: Microphysical Properties and Their Relationships With
     Aerosols, Journal of Geophysical Research: Atmospheres, 124, 1798–1822, https://doi.org/https://doi.org/10.1029/2018JD029802, 2019.

780 Komppula, M., Lihavainen, H., Kerminen, V.-M., Kulmala, M., and Viisanen, Y.: Measurements of cloud droplet acti-
     vation of aerosol particles at a clean subarctic background site, Journal of Geophysical Research: Atmospheres, 110,
     https://doi.org/https://doi.org/10.1029/2004JD005200, 2005.

Korhonen, H., Carslaw, K. S., Spracklen, D. V., Mann, G. W., and Woodhouse, M. T.: Influence of oceanic dimethyl sulfide emissions on
     cloud condensation nuclei concentrations and seasonality over the remote Southern Hemisphere oceans: A global model study, Journal of
785 Geophysical Research Atmospheres, 113, https://doi.org/10.1029/2007JD009718, 2008a.

Korhonen, H., Carslaw, K. S., Spracklen, D. V., Ridley, D. A., and Ström, J.: A global model study of processes controlling aerosol size dis-
     tributions in the Arctic spring and summer, Journal of Geophysical Research: Atmospheres, 113, https://doi.org/10.1029/2007JD009114,
     2008b.

Kulmala, M., Lehtinen, K. E. J., and Laaksonen, A.: Atmospheric Chemistry and Physics Cluster activation theory as an explanation of
790 the linear dependence between formation rate of 3 nm particles and sulphuric acid concentration, Atmos. Chem. Phys, 6, 787–793,
     www.atmos-chem-phys.net/6/787/2006/, 2006.

Kupiszewski, P., Leck, C., Tjernström, M., Sjogren, S., Sedlar, J., Graus, M., Müller, M., Brooks, B., Swietlicki, E., Norris, S., and Hansel, A.:
     Vertical profiling of aerosol particles and trace gases over the central Arctic Ocean during summer, Atmospheric Chemistry and Physics,
     13, 12 405–12 431, https://doi.org/10.5194/acp-13-12405-2013, 2013.

795 Lawler, M. J., Saltzman, E. S., Karlsson, L., Zieger, P., Salter, M., Baccarini, A., Schmale, J., and Leck, C.: New Insights Into the
     Composition and Origins of Ultrafine Aerosol in the Summertime High Arctic, Geophysical Research Letters, 48, e2021GL094 395,
     https://doi.org/https://doi.org/10.1029/2021GL094395, e2021GL094395 2021GL094395, 2021.

Leck, C. and Bigg, E. K.: New particle formation of marine biological origin, vol. 44, pp. 570–577, https://doi.org/10.1080/02786826.2010.481222, 2010.

800 Leck, C. and Svensson, E.: Importance of aerosol composition and mixing state for cloud droplet activation over the Arctic pack ice in summer, Atmospheric Chemistry and Physics, 15, 2545–2568, https://doi.org/10.5194/acp-15-2545-2015, 2015.

Loewe, K., Ekman, A. M. L., Paukert, M., Sedlar, J., Tjernström, M., and Hoose, C.: Modelling micro- and macrophysical contributors to the dissipation of an Arctic mixed-phase cloud during the Arctic Summer Cloud Ocean Study (ASCOS), Atmospheric Chemistry and Physics, 17, 6693–6704, https://doi.org/10.5194/acp-17-6693-2017, 2017.

805 Lubin, D. and Vogelmann, A. M.: A climatologically significant aerosol longwave indirect effect in the Arctic, Nature, 439, 453–456, https://doi.org/10.1038/nature04449, 2006.

Mann, G. W., Carslaw, K. S., Spracklen, D. V., Ridley, D. A., Manktelow, P. T., Chipperfield, M. P., Pickering, S. J., and Johnson, C. E.: Description and evaluation of GLOMAP-mode: a modal global aerosol microphysics model for the UKCA composition-climate model, Geoscientific Model Development, 3, 519–551, https://doi.org/10.5194/gmd-3-519-2010, 2010.

810 Marle, M. J. V., Kloster, S., Magi, B. I., Marlon, J. R., Daniau, A. L., Field, R. D., Arneth, A., Forrest, M., Hantson, S., Kehrwald, N. M., Knorr, W., Lasslop, G., Li, F., Mangeon, S., Yue, C., Kaiser, J. W., and Werf, G. R. V. D.: Historic global biomass burning emissions for CMIP6 (BB4CMIP) based on merging satellite observations with proxies and fire models (1750-2015), Geoscientific Model Development, 10, 3329–3357, https://doi.org/10.5194/gmd-10-3329-2017, 2017.

Mauritsen, T., Sedlar, J., Tjernström, M., Leck, C., Martin, M., Shupe, M., Sjogren, S., Sierau, B., Persson, P. O. G., Brooks, I. M., and Swi-
815 etlicki, E.: An Arctic CCN-limited cloud-aerosol regime, Atmospheric Chemistry and Physics, 11, 165–173, https://doi.org/10.5194/acp-11-165-2011, 2011.

Merikanto, J., Spracklen, D. V., Mann, G. W., Pickering, S. J., and Carslaw, K. S.: Atmospheric Chemistry and Physics Impact of nucleation on global CCN, Atmos. Chem. Phys, 9, 8601–8616, www.atmos-chem-phys.net/9/8601/2009/, 2009.

Metzger, A., Verheggen, B., Dommen, J., Duplissy, J., Prevot, A. S., Weingartner, E., Riipinen, I., Kulmala, M., Spracklen, D. V., Carslaw,
820 K. S., and Baltensperger, U.: Evidence for the role of organics in aerosol particle formation under atmospheric conditions, Proceedings of the National Academy of Sciences of the United States of America, 107, 6646–6651, https://doi.org/10.1073/pnas.0911330107, 2010.

Morgenstern, O., Braesicke, P., O'connor, F. M., Bushell, A. C., Johnson, C. E., Osprey, S. M., and Pyle, J. A.: Evaluation of the new UKCA climate-composition model-Part 1: The stratosphere, Geosci. Model Dev, 2, 43–57, www.geosci-model-dev.net/2/43/2009/, 2009.

Mulcahy, J. P., Johnson, C., Jones, C. G., Povey, A. C., Scott, C. E., Sellar, A., Turnock, S. T., Woodhouse, M. T., Abraham, N. L., Andrews,
825 M. B., Bellouin, N., Browse, J., Carslaw, K. S., Dalvi, M., Folberth, G. A., Glover, M., Grosvenor, D. P., Hardacre, C., Hill, R., Johnson, B., Jones, A., Kipling, Z., Mann, G., Mollard, J., O'Connor, F. M., Palmiéri, J., Reddington, C., Rumbold, S. T., Richardson, M., Schutgens, N. A., Stier, P., Stringer, M., Tang, Y., Walton, J., Woodward, S., and Yool, A.: Description and evaluation of aerosol in UKESM1 and HadGEM3-GC3.1 CMIP6 historical simulations, Geoscientific Model Development, 13, 6383–6423, https://doi.org/10.5194/gmd-13-6383-2020, 2020.

830 Notz, D. and Stroeve, J.: The Trajectory Towards a Seasonally Ice-Free Arctic Ocean, Current Climate Change Reports, 4, 407–416, https://doi.org/10.1007/s40641-018-0113-2, 2018.

O'Connor, F. M., Johnson, C. E., Morgenstern, O., Abraham, N. L., Braesicke, P., Dalvi, M., Folberth, G. A., Sanderson, M. G., Telford, P. J., Voulgarakis, A., Young, P. J., Zeng, G., Collins, W. J., and Pyle, J. A.: Evaluation of the new UKCA climate-composition model-Part 2: The troposphere, Geoscientific Model Development, 7, 41–91, https://doi.org/10.5194/gmd-7-41-2014, 2014.

10.5194/egusphere-2022-1079

Pastore, M. and Calcagnì, A.: Measuring distribution similarities between samples: A distribution-free overlapping index, Frontiers in Psychology, 10, https://doi.org/10.3389/fpsyg.2019.01089, 2019.

Pöhlker, M. L., Zhang, M., Campos Braga, R., Krüger, O. O., Pöschl, U., and Ervens, B.: Aitken mode particles as CCN in aerosol- and updraft-sensitive regimes of cloud droplet formation, Atmospheric Chemistry and Physics, 21, 11 723–11 740, https://doi.org/10.5194/acp-21-11723-2021, 2021.

Randerson, J. T., Liu, H., Flanner, M. G., Chambers, S. D., Jin, Y., Hess, P. G., Pfister, G., Mack, M. C., Treseder, K. K., Welp, L. R., Chapin, F. S., Harden, J. W., Goulden, M. L., Lyons, E., Neff, J. C., Schuur, E. A., and Zender, C. S.: The impact of boreal forest fire on climate warming, Science, 314, 1130–1132, https://doi.org/10.1126/science.1132075, 2006.

Rantanen, M., Karpechko, A. Y., Lipponen, A., Nordling, K., Hyvärinen, O., Ruosteenoja, K., Vihma, T., and Laaksonen, A.: The Arctic has warmed nearly four times faster than the globe since 1979, Communications Earth Environment, 3, 168, https://doi.org/10.1038/s43247-022-00498-3, 2022.

Schmale, J. and Baccarini, A.: Progress in Unraveling Atmospheric New Particle Formation and Growth Across the Arctic, Geophysical Research Letters, 48, https://doi.org/https://doi.org/10.1029/2021GL094198, 2021.

Schmale, J., Zieger, P., and Ekman, A. M.: Aerosols in current and future Arctic climate, Nature Climate Change, 11, 95–105, https://doi.org/10.1038/s41558-020-00969-5, 2021.

Schmale, J., Sharma, S., Decesari, S., Pernov, J., Massling, A., Hansson, H.-C., von Salzen, K., Skov, H., Andrews, E., Quinn, P. K., Upchurch, L. M., Eleftheriadis, K., Traversi, R., Gilardoni, S., Mazzola, M., Laing, J., and Hopke, P.: Pan-Arctic seasonal cycles and long-term trends of aerosol properties from 10 observatories, Atmospheric Chemistry and Physics, 22, 3067–3096, https://doi.org/10.5194/acp-22-3067-2022, 2022.

Sedlar, J., Tjernström, M., Mauritsen, T., Shupe, M. D., Brooks, I. M., Persson, P. O. G., Birch, C. E., Leck, C., Sirevaag, A., and Nicolaus, M.: A transitioning Arctic surface energy budget: the impacts of solar zenith angle, surface albedo and cloud radiative forcing, Climate Dynamics, 37, 1643–1660, https://doi.org/10.1007/s00382-010-0937-5, 2011.

Sellar, A. A., Jones, C. G., Mulcahy, J. P., Tang, Y., Yool, A., Wiltshire, A., O'Connor, F. M., Stringer, M., Hill, R., Palmieri, J., Woodward, S., de Mora, L., Kuhlbrodt, T., Rumbold, S. T., Kelley, D. I., Ellis, R., Johnson, C. E., Walton, J., Abraham, N. L., Andrews, M. B., Andrews, T., Archibald, A. T., Berthou, S., Burke, E., Blockley, E., Carslaw, K., Dalvi, M., Edwards, J., Folberth, G. A., Gedney, N., Griffiths, P. T., Harper, A. B., Hendry, M. A., Hewitt, A. J., Johnson, B., Jones, A., Jones, C. D., Keeble, J., Liddicoat, S., Morgenstern, O., Parker, R. J., Predoi, V., Robertson, E., Siahaan, A., Smith, R. S., Swaminathan, R., Woodhouse, M. T., Zeng, G., and Zerroukat, M.: UKESM1: Description and Evaluation of the U.K. Earth System Model, Journal of Advances in Modeling Earth Systems, 11, 4513–4558, https://doi.org/https://doi.org/10.1029/2019MS001739, 2019.

Sharma, S., Barrie, L. A., Magnusson, E., Brattstr om, G., Leaitch, W. R., Steffen, A., and Landsberger, S.: A Factor and Trends Analysis of Multidecadal Lower Tropospheric Observations of Arctic Aerosol Composition, Black Carbon, Ozone, and Mercury at Alert, Canada, Journal of Geophysical Research: Atmospheres, 124, 14 133–14 161, https://doi.org/10.1029/2019JD030844, 2019.

Shepherd, A., Ivins, E. R., A, G., Barletta, V. R., Bentley, M. J., Bettadpur, S., Briggs, K. H., Bromwich, D. H., Forsberg, R., Galin, N., Horwath, M., Jacobs, S., Joughin, I., King, M. A., Lenaerts, J. T. M., Li, J., Ligtenberg, S. R. M., Luckman, A., Luthcke, S. B., McMillan, M., Meister, R., Glenn, M., Mouginot, J., Muir, A., Nicolas, J. P., Paden, J., Payne, A. J., Pritchard, H., Rignot, E., Rott, H., Sørensen, L. S., Scambos, T. A., Scheuchl, B., Schrama, E. J. O., Smith, B., Sundal, A. V., van Angelen, J. H., van de Berg, W. J., van den Broeke, M. R., Vaughan, D. G., Velicogna, I., Wahr, J., Whitehouse, P. L., Wingham, D. J., Yi, D., Young, D., and Zwally, H. J.: A Reconciled Estimate of Ice-Sheet Mass Balance, Science, 338, https://doi.org/10.1126/science.1228102, 2012.

Shupe, M. D.: Clouds at Arctic Atmospheric Observatories. Part II: Thermodynamic Phase Characteristics, Journal of Applied Meteorology and Climatology, 50, 645–661, https://doi.org/10.1175/2010JAMC2468.1, 2011.

875 Shupe, M. D. and Intrieri, J. M.: Cloud Radiative Forcing of the Arctic Surface: The Influence of Cloud Properties, Surface Albedo, and Solar Zenith Angle, Journal of Climate, 17, 616 – 628, https://doi.org/10.1175/1520-0442(2004)017<0616:CRFOTA>2.0.CO;2, 2004.

Sindelarova, K., Granier, C., Bouarar, I., Guenther, A., Tilmes, S., Stavrakou, T., Muller, J.-F., Kuhn, U., Stefani, P., and Knorr, W.: Global data set of biogenic VOC emissions calculated by the MEGAN model over the last 30 years, Atmospheric Chemistry and Physics, 14, 9317–9341, https://doi.org/10.5194/acp-14-9317-2014, 2014.

880 Sipil a, M., Sarnela, N., Jokinen, T., Henschel, H., Junninen, H., Kontkanen, J., Richters, S., Kangasluoma, J., Franchin, A., Per akyl a, O., Rissanen, M. P., Ehn, M., Vehkam aki, H., Kurten, T., Berndt, T., Pet aj a, T., Worsnop, D., Ceburnis, D., Kerminen, V. M., Kulmala, M., and O'Dowd, C.: Molecular-scale evidence of aerosol particle formation via sequential addition of HIO3, Nature, 537, 532–534, https://doi.org/10.1038/nature19314, 2016.

Solomon, A., Shupe, M. D., Persson, P. O. G., and Morrison, H.: Moisture and dynamical interactions maintaining decoupled Arc-
885 tic mixed-phase stratocumulus in the presence of a humidity inversion, Atmospheric Chemistry and Physics, 11, 10 127–10 148, https://doi.org/10.5194/acp-11-10127-2011, 2011.

Spracklen, D. V., Carslaw, K. S., Kulmala, M., Kerminen, V.-M., Mann, G. W., and Sihto, S.-L.: Atmospheric Chemistry and Physics, European Geosciences Union, 6, 5631–5648, www.atmos-chem-phys.net/6/5631/2006/, 2006.

Stevens, R. G., Loewe, K., Dearden, C., Dimitrelos, A., Possner, A., Eirund, G. K., Raatikainen, T, Hill, A. A., Shipway, B. J., Wilkinson,
890 J., Romakkaniemi, S., Tonttila, J., Laaksonen, A., Korhonen, H., Connolly, P., Lohmann, U., Hoose, C., Ekman, A. M. L., Carslaw, K. S., and Field, P. R.: A model intercomparison of CCN-limited tenuous clouds in the high Arctic, Atmospheric Chemistry and Physics, 18, 11 041–11 071, https://doi.org/10.5194/acp-18-11041-2018, 2018.

Stohl, A.: Characteristics of atmospheric transport into the Arctic troposphere, Journal of Geophysical Research: Atmospheres, 111, https://doi.org/10.1029/2005JD006888, 2006.

895 Ström, J., Umegård, J., Tørseth, K., Tunved, P., Hansson, H.-C., Holmén, K., Wismann, V., Herber, A., and König-Langlo, G.: One year of particle size distribution and aerosol chemical composition measurements at the Zeppelin Station, Svalbard, March 2000–March 2001, Physics and Chemistry of the Earth, Parts A/B/C, 28, 1181 – 1190, https://doi.org/https://doi.org/10.1016/j.pce.2003.08.058, 2003.

Struthers, H., Ekman, A. M. L., Glantz, P., Iversen, T., Kirkevåg, A., Mårtensson, E. M., Seland, Ø., and Nilsson, E. D.: The effect of sea ice loss on sea salt aerosol concentrations and the radiative balance in the Arctic, Atmospheric Chemistry and Physics, 11, 3459–3477,
900 https://doi.org/10.5194/acp-11-3459-2011, 2011.

Tjernström, M., Leck, C., Birch, C. E., Bottenheim, J. W., Brooks, B. J., Brooks, I. M., Bäcklin, L., Chang, R. Y., Leeuw, G. D., Liberto, L. D., Rosa, S. D. L., Granath, E., Graus, M., Hansel, A., Heintzenberg, J., Held, A., Hind, A., Johnston, P., Knulst, J., Martin, M., Matrai, P. A., Mauritsen, T., Müller, M., Norris, S. J., Orellana, M. V., Orsini, D. A., Paatero, J., Persson, P. O., Gao, Q., Rauschenberg, C., Ristovski, Z., Sedlar, J., Shupe, M. D., Sierau, B., Sirevaag, A., Sjogren, S., Stetzer, O., Swietlicki, E., Szczodrak, M., Vaattovaara, P.,
905 Wahlberg, N., Westberg, M., and Wheeler, C. R.: The Arctic Summer Cloud Ocean Study (ASCOS): Overview and experimental design, Atmospheric Chemistry and Physics, https://doi.org/10.5194/acp-14-2823-2014, 2014.

Tunved, P., Ström, J., and Krejci, R.: Arctic aerosol life cycle: linking aerosol size distributions observed between 2000 and 2010 with air mass transport and precipitation at Zeppelin station, Ny-Ålesund, Svalbard, Atmospheric Chemistry and Physics, 13, 3643–3660, https://doi.org/10.5194/acp-13-3643-2013, 2013.

910 Vehkamäki, H., Kulmala, M., Napari, I., Lehtinen, K. E. J., Timmreck, C., Noppel, M., and Laaksonen, A.: An improved parameteriza-
     tion for sulfuric acid–water nucleation rates for tropospheric and stratospheric conditions, Journal of Geophysical Research, 107, 4622,
     https://doi.org/10.1029/2002JD002184, 2002.

     Vüllers, J., Achtert, P., Brooks, I., Tjernström, M., Prytherch, J., and III, R. N.: Meteorological and cloud conditions during the Arctic Ocean
     2018 expedition, Atmospheric Chemistry and Physics, pp. 1–43, https://doi.org/10.5194/acp-2020-219, 2020.

915 Walker, X. J., Baltzer, J. L., Cumming, S. G., Day, N. J., Ebert, C., Goetz, S., Johnstone, J. F., Potter, S., Rogers, B. M., Schuur, E. A.,
     Turetsky, M. R., and Mack, M. C.: Increasing wildfires threaten historic carbon sink of boreal forest soils, Nature, 572, 520–523,
     https://doi.org/10.1038/s41586-019-1474-y, 2019.

     Walters, D., Baran, A. J., Boutle, I., Brooks, M., Earnshaw, P., Edwards, J., Furtado, K., Hill, P., Lock, A., Manners, J., Morcrette, C.,
     Mulcahy, J., Sanchez, C., Smith, C., Stratton, R., Tennant, W., Tomassini, L., Weverberg, K. V., Vosper, S., Willett, M., Browse, J., Bushell,
920 A., Carslaw, K., Dalvi, M., Essery, R., Gedney, N., Hardiman, S., Johnson, B., Johnson, C., Jones, A., Jones, C., Mann, G., Milton, S.,
     Rumbold, H., Sellar, A., Ujiie, M., Whitall, M., Williams, K., and Zerroukat, M.: The Met Office Unified Model Global Atmosphere
     7.0/7.1 and JULES Global Land 7.0 configurations, Geoscientific Model Development, 12, 1909–1963, https://doi.org/10.5194/gmd-12-
     1909-2019, 2019.

     Willis, M. D., K ollner, F., Burkart, J., Bozem, H., Thomas, J. L., Schneider, J., Aliabadi, A. A., Hoor, P. M., Schulz, H., Herber, A. B.,
925 Leaitch, W. R., and Abbatt, J. P.: Evidence for marine biogenic influence on summertime Arctic aerosol, Geophysical Research Letters,
     44, 6460–6470, https://doi.org/10.1002/2017GL073359, 2017.

     Willis, M. D., Leaitch, W. R., and Abbatt, J. P.: Processes Controlling the Composition and Abundance of Arctic Aerosol, Reviews of
     Geophysics, 56, 621–671, https://doi.org/10.1029/2018RG000602, 2018.

     Zhang, R., Wang, H., Fu, Q., Rasch, P. J., and Wang, X.: Unraveling driving forces explaining significant reduction in satellite-inferred Arctic
930 surface albedo since the 1980s, Proceedings of the National Academy of Sciences of the United States of America, 116, 23 947–23 953,
     https://doi.org/10.1073/pnas.1915258116, 2019.